OPTIMIZATION FRAMEWORK FOR MATERIAL PARAMETER IDENTIFICATION APPLIED TO HOT FORGING PROCESS.

Thesis submitted by:

M. Sc. Diego Armando Gomez Marquez

HIROSHIMA UNIVERSITY

In partial fulfillment of the Requirements of the Hiroshima University for the Degree of Doctor of Philosophy.

Hiroshima University

Graduate School of Advanced Science and Engineering

Higashihiroshima City

2024

OPTIMIZATION FRAMEWORK FOR MATERIAL PARAMETER IDENTIFICATION APPLIED TO HOT FORGING PROCESS.

Thesis submitted by:

M. Sc. Diego Armando Gomez Marquez

In partial fulfillment of the Requirements of the Hiroshima University for the Degree of Doctor of Philosophy.

Advisors:

Prof. Ryutaro Hino (Hiroshima University)

Prof. Elias Ledesma (Universidad de Guanajuato)

Graduate School of Advanced Science and Engineering

Hiroshima University

Higashihiroshima City

2024

Table of Contents

List of Figures

List of Tables

List of Appendix

INTRODUCTION

The automotive industry relies heavily on simulation methods to validate designs, processes, and optimization. There are several reasons for this fact: the computational power is increasing exponentially, the simulation techniques are becoming more accurate, and most importantly, the cost-benefit of using simulation has reached a high level. All these factors have contributed to reducing the development cost, producing an optimal process, and minimizing the time to reach the market.

The simulation accuracy achieved high maturity, mainly based on the improvement of the constitutive model. This model allows for the calculation of stress based on other factors, such as temperature, strain rate, and strain. Nowadays, there are plenty of constitutive models that allow model-specific phenomena such as elastic plasticity, hyper-elasticity, creep, and the Bauschinger effect. However, the accuracy of the outcome of these models relies on the accuracy of the parameter feeding the equation.

To achieve good accuracy of the inputs for material model, it is needed to perform a constitutive analysis of each material intended to be used in a design the consequently, as input in a simulation model. This allowed us to understand the behavior of the material and, therefore, to choose an adequate constitutive model. Then, the material parameters must be determined, which is also known as *material parameter identification*. Finally, the constitutive model can be used in the simulation model by feeding the determined parameters.

In this study, an optimization framework was developed to determine the parameters for the constitutive equation used in hot forging modeling. To test this framework, 38MnVS6 steel was used, and two commonly used constitutive models were used: Johnson-Cook and the Hensel-Spittel models. The state-of-the-art regarding material behavior at high temperatures, a type of model, and optimization techniques are provided in Chapter 2. Subsequently, the material, methods and experimental description, along with the constitutive analysis base on the Arrhenius-type equation is given in Chapter 3. Parameter identification is demonstrated in Chapter 4, which also shows a new objective function proposed in this study to reduce the number of iterations during the optimization procedure. Finally, a conclusion and an outlook are provided in Chapter 5.

1. PROBLEM STATEMENT

1.1. Hypothesis

Introducing a logarithmic function into the objective function employed in the parameter identification process for the constitutive equation commonly used to model the plastic flow stress in hot metal forming applications has the potential to significantly improve the optimization process. This is based on the well-known characteristic of logarithmic functions, which exhibit rapid changes in the output for minimal input variations.

Based on this property of the logarithmic functions, we anticipate a substantial reduction in the number of iterations required to achieve convergence for parameter identification. The primary objective of this optimization is to minimize the error between the outcomes of the constitutive equation and experimentally measured flow stress. Currently, the least-squares method is the most widely used approach in this domain, making it an ideal benchmark for comparison with the proposed function.

1.2. Objective

To develop a methodology framework based on the implementation of the logarithmic function within the parameter identification process with the goal of improving the accuracy and efficiency of modeling plastic flow stress in hot metal forming. As a result, a procedure that can be easily implemented for industrial applications is expected, allowing a reduction in the identification time for constitutive modeling.

1.3. Justification

Currently, the time frame for the Design and Development (D&D) of new products is getting shorter and shorter. This mainstream has been supported by the integration of advanced computer-aided design (CAD) software and computer-aided engineering (CAE) software. Moreover, manufacturing systems, such as additive manufacturing, have experienced significant improvements. Furthermore, new materials have been developed, reaching yield limits over 1000 MPa, which has been a key part of the lightweight strategies in the automotive industry: reducing mass by replacing material with other more resistant materials, which gives similar or even better performance, and maintains a lower mass.

The automotive industry extensively uses metal forming processes to manufacture vehicle components. This is due to the metal forming ability to produce at a high rate while maintaining a low piece cost. For instance, sheet metal forming processes are used to

produce body in white (BIW) parts, whereas the forging process is used to produce engine and transmission parts, such as crankshafts, connecting roads, and gears. Regardless of the material and function of the components, CAD and CAE usage is involved because of the conceptualization, virtual design validation, and process design. This allows engineers to significantly reduce the number of iterations required to complete and validate a design.

The output reliability of the CAE simulation, such as a Finite Element Analysis (FEA), strongly depends on the quality of the inputs, that is, the geometry and its discretization (mesh), boundary condition (loads and constraints), and constitutive models (and its parameters). Therefore, it is necessary to have an accurate model if the design relies on the results. This study focuses on generating an optimization framework that allows the determination of parameters for a constitutive model and quickly and accurately estimates its parameters. The main objective is to generate a framework intended to provide fast and reliable constitutive parameters for industrial applications, such that the forging process can be analyzed properly during the design stages or for troubleshooting during production. Furthermore, product design can be optimized in addition to other aspects, such as process optimization (material utilization) and tool life optimization.

2. BACKGROUND AND STATE OF THE ART

Metal-forming applications have been widely used for the massive production of goods since the Second Industrial Revolution. In metal-forming applications, material description has been one of the most challenging aspects; several efforts have been made on this aspect since the last century. Originally, metal-forming processes were developed through trial and error, relying on experience. Numerical simulations have been applied to process modeling as their capabilities to capture complex phenomena have been increasing rapidly and are still in progress. Among the advances in numerical simulation, the constitutive equation for material behavior description stands out. The complexity of the material behavior is transferred to the mathematical formulation of these equations, which are later solved by simulation. Therefore, material parameter identification for constitutive equations is a central aspect of process modeling.

In this chapter, an introductory background is given, stating some basics of the metal forming processes, including a central aspect of these processes, that is, the material behavior and its characterization. Furthermore, a quick review of the optimization techniques is provided to arrive at material parameter identification, the major topic addressed in this work.

2.1. Metal forming processes

In modern manufacturing, there are two methods to classify processes based on material deformation: property-driven and geometry-driven. Metal-forming techniques fall into the geometry-driven category, which consists of transferring a geometry from a tool or die into a workpiece called a blank (in sheet metal) or billet (in bulk-forming operations). The initial geometries are generally simple, such as a sheet blank or a cylinder, and then plastically deformed by the load applied by tools or dies to obtain the final shape, as shown in Figure 1.

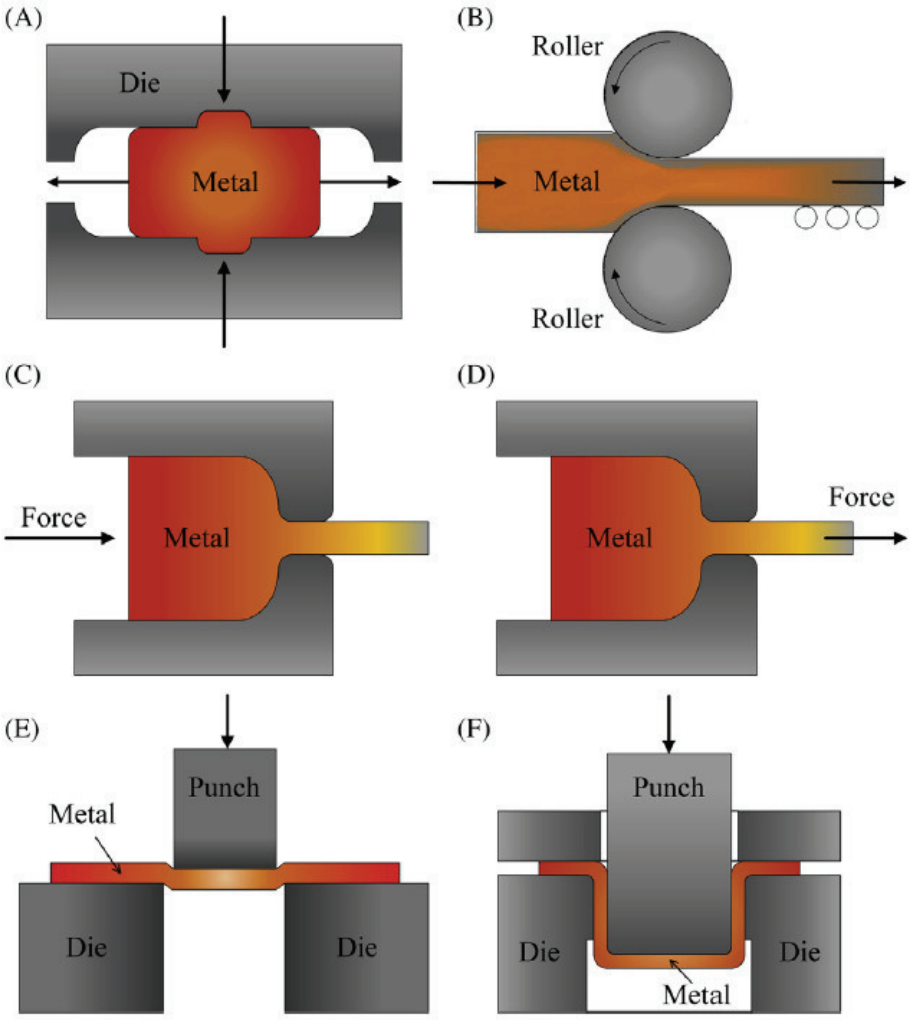

Figure 1. Essential bulk and sheet-metal forming processes: (A) forging; (B) rolling; (C) extruding; (D) drawing; (E) shearing; (F) stamping. [1].

Reprinted with permission from Elsevier.

For all processes, there are some input parameters and characteristics, such as material, process routing, process window, tooling design, and equipment. After the process is completed, there are specific outputs such as product geometry, microstructure, defects, cost, and environmental impact [2]. The amount of production per year has increased in recent years, even though some relocation has occurred, as reported by EUROFORGE [3]. These statistics show the increment in production volume per year; therefore, this involves significant challenges from different standpoints, such as engineering, design, and logistics, among the other domains involved in the supply chain.

To reduce the cost and time impact due to trials, process modeling is an advantageous approach because it offers several capabilities, as Dixit [4] pointed out: (1) the required deformation load, (2) energy consumption in the process, (3) stresses on the dies and tools,

(4) defects in the process, (5) quality of the product, particularly in terms of dimensional accuracy and surface integrity, (6) properties of the product, (7) stress, strain, strain rate, and temperature distribution in the product as well as tooling, and (8) life assessment of the tooling and machine. This information can be obtained from a process model, which is an essential step before optimization is implemented. Recent challenges in bulk metal forming are mainly driven by the necessity of improvements in precision forming, as pointed out by Gronostajski et al. [5], which is more challenging because it is susceptible to the tool geometry and billet size. Therefore, the accuracy of tool wear, material flow, and process parameters is a central aspect to consider during the design and development of a product.

In forming simulations and obtaining accurate stress and strain fields, the FEA code requires secure input data, such as geometry, mesh, nonlinear material behavior laws (also known as constitutive equations), loading cases, and friction laws. [6]. All of these aspects have a significant effect on the model outcome, and their correct determination is crucial for proper modeling. For accurate inputs, two approaches are typically used in engineering, as shown in Figure 2: The first is called Finite Element Model Updating (FEMU), where parameters are changed until a good fit is obtained for one or more variables, such as load and stain. The second approach is called the Virtual Field Method (VFM), which uses a balance between the internal and external virtual work to fit the parameters. The following subsection briefly introduces the constitutive equation commonly used in hot forging and the process effect on material behavior, as well as friction and tribology at high temperatures.

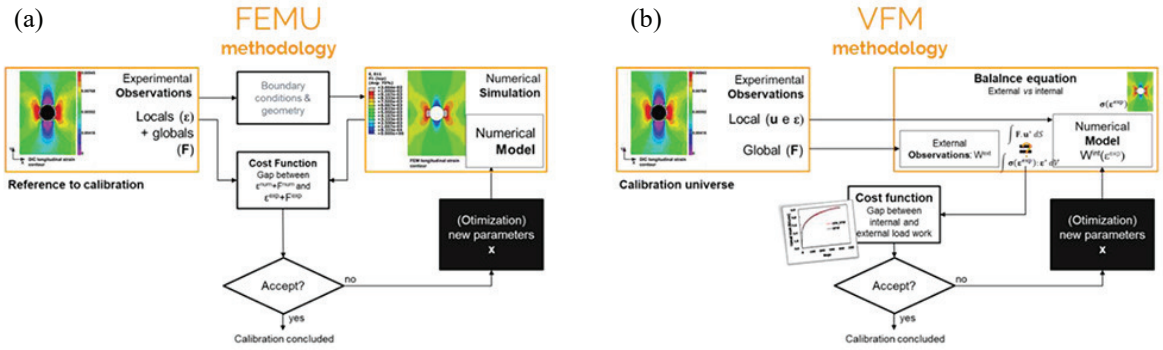

Figure 2. General methodologies for parameter identification: (a) Finite Element Model Updating (FEMU) and (b) Virtual Field Method (VFM) [6].

Reproduced with permission from Springer.

2.2. Material behavior at high temperature

Metals deformed at high temperatures exhibit complex behavior; they are a mixture of hardening and softening that occur simultaneously. However, depending on the

temperature and amount of deformation, either hardening or softening is dominant. In general, when metals are deformed at elevated temperatures, they exhibit four stages, as shown in Figure 3. In phase I, work hardening (WH) occurs, and its rate is higher than the softening rate induced by dynamic recovery (DRV); therefore, the stress increases rapidly. During stage II, known as the transition, there is competition among the effects of WH, DRV, and dynamic recrystallization (DRX), where the stress still increases, although it does slowly. During stage III, softening occurs, and the stress drops rapidly owing to DRX. Finally, in stage IV, a steady state is reached owing to a balance between DRV and DRX [7].

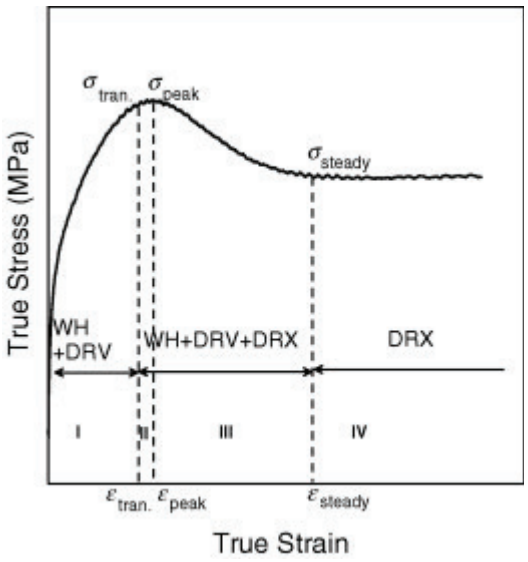

Figure 3. Typical flow stress curve at the elevated temperature [7].

Reproduced with permission from Elsevier.

These stages depend on the deformation temperature, strain rate, and chemical composition. During dynamic recovery, the original grains became increasingly strained, but the sub-boundaries remained equiaxed, as shown in Figure 4 (a). With further deformation, more potential nuclei were activated and new recrystallized grains appeared [8], as shown in Figure 4 (b).

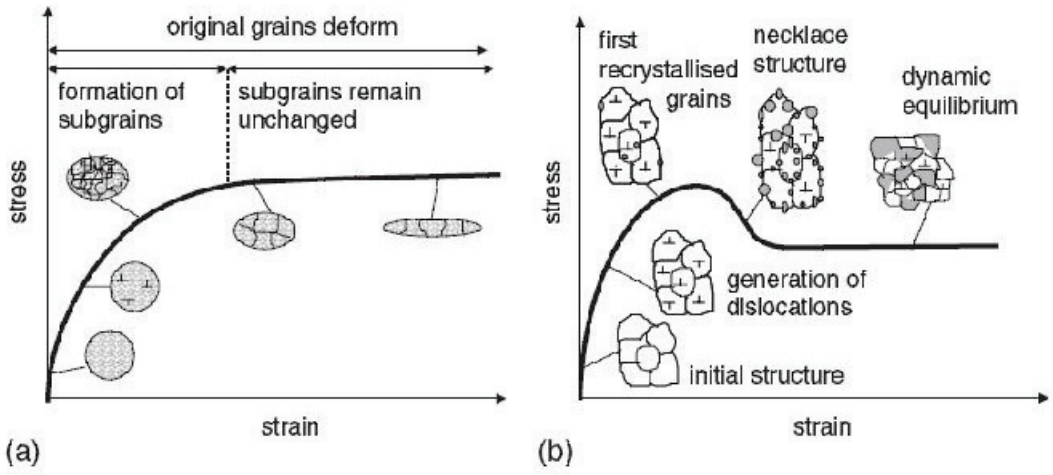

Figure 4. Evolution of microstructure during (a) hot deformation of a material showing recovery and (b) continuous [8].

There are four characteristic points of interest in a typical stress-strain response curve at high temperature, as can be seen in Figure 5: σ_0 is when the plastic deformation starts, σ_p is the maximum (peak) stress value achieved ,and its corresponding peak strain value ε_0, then the stress decreases until the inflection point σ_i is observed at its corresponding inflection stain ε_i; finally the steady state is achieve, dnoted by the pair $(\sigma_{ss}, \varepsilon_{ss})$.

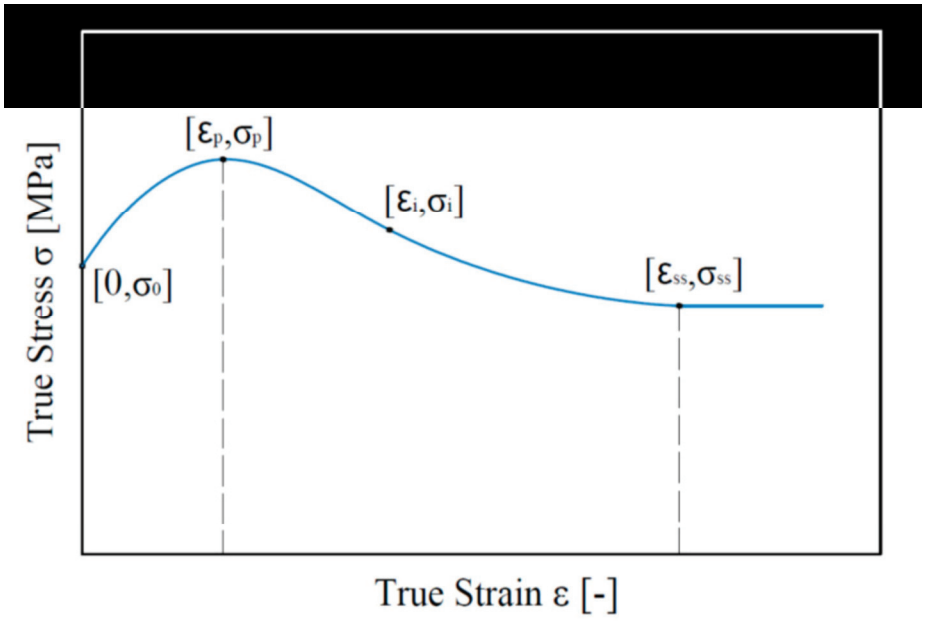

Figure 5 Typical high-temperature true stress-strain response under compression [9].

Using a phenomenological standpoint, the metals flow stress σ can be expressed as function of temperature T, strain ε, and strain rate $\dot{\varepsilon}$, as is expressed by Equation 1. In hot forging of metals, when temperatures above the recrystallization point are used, the effect of strain is negligible [2].

$$\sigma = f(\varepsilon, T, \dot{\varepsilon}) \qquad \textit{Equation 1}$$

Let us now consider 05Cr17Ni4Cu4Nb steel deformed at high temperature and compressed in the cylindrical test (also known as the upsetting test). When the temperature is constant and the strain rate changes (but remains constant during the test), the effect is shown in Figure 6 (a), where the flow stress increases with the strain rate. On the other hand, when the strain rate was maintained constant and the test temperature changed (but remained constant during the test), as shown in Figure 6 (b), the flow stress increased when the deformation temperature decreased.

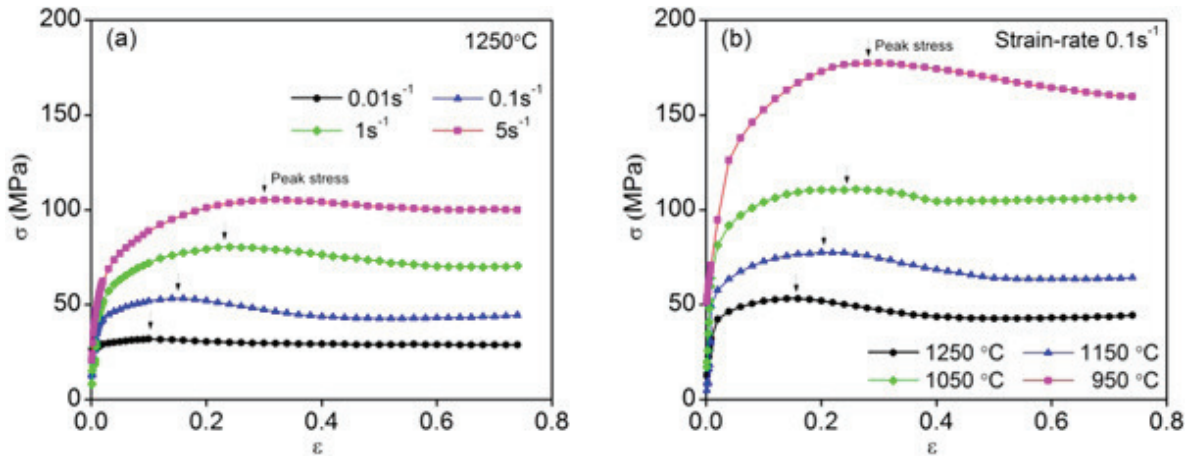

Figure 6.Flow stress of 05Cr17Ni4Cu4Nb steel (a) at 1250 °C and (b) at 0.1 s^{-1} *[10].*

2.3.Optimizations methods

The complexity of a problem is driven by the number of variables required to properly model it. This can lead to the existence of several local minima, and it is the user that needs to evaluate the result. There are different methods suitable for each type of problem [11]: simple search, gradient-based, and evolutionary. Furthermore, based on the type of search, some authors distinguish between local, global, and hybrid searches [12]. In Figure 7, a classification based on the type of search is given; nevertheless, this classification does not account for all methods, nor is it mentioned in the discussion. Moreover, as pointed out by

Wolpert and Macready [13], there is no ultimate optimization method that solves all problems equally efficiently, and it is dangerous to evaluate an optimization method based on a small sample of problems.

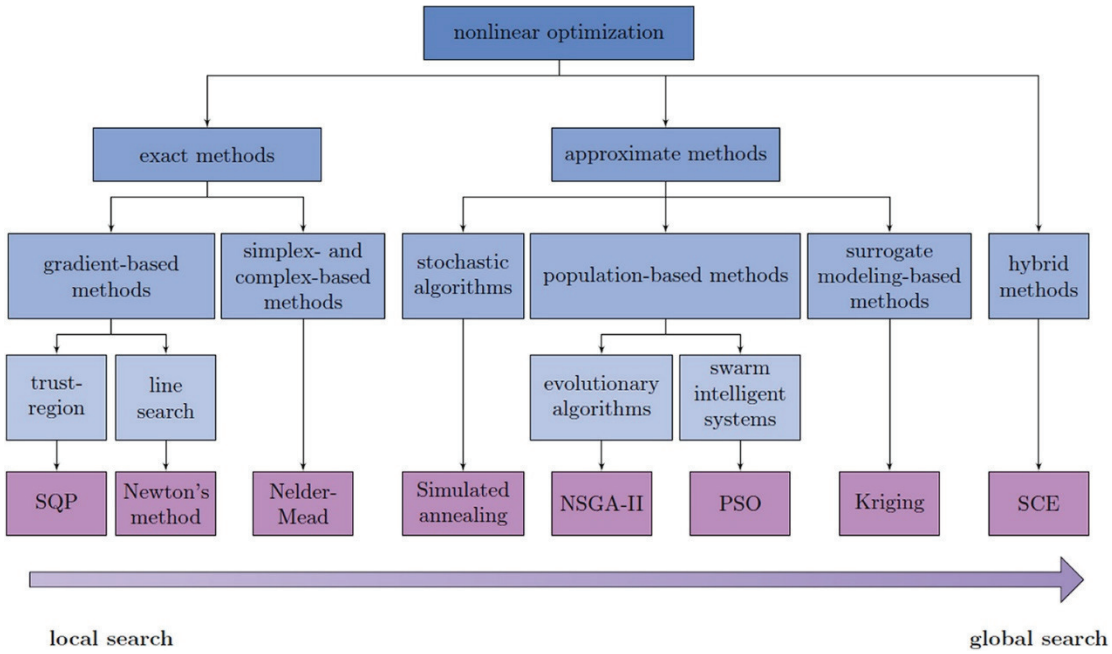

Figure 7. Overview and classification of different optimization methods [12].

Reprinted with permission from Elsevier.

2.3.1. Simple searching methods

Simple search methods are also known as gradient-free or direct search methods. They are based only on the evaluation of the objective function (OF), which makes them computationally fast, easy to implement, and useful when the gradient is difficult to calculate. However, these methods can easily fall into local minima, which also means that they are highly sensitive to the starting point and user experience. There are different algorithms for this method, including Rosenbrock, Simplex, and Powell.

To explain gradient-free methods, we can mention the Nelder-Mead [14] of the Simplex Algorithm (NMSA), which finds a local minimum to an objective function (OF). For each iteration, the algorithm performed four operations: reflection, expansion, contraction, and similarity transformation. The first step was to change the worst point with a point reflected through the centroid in the opposite direction. If this point is better than the current point, the region is expanded along this line, as Figure 8 shows. However, if this reflected point does not provide a better result, the region is contracted towards the best current point.

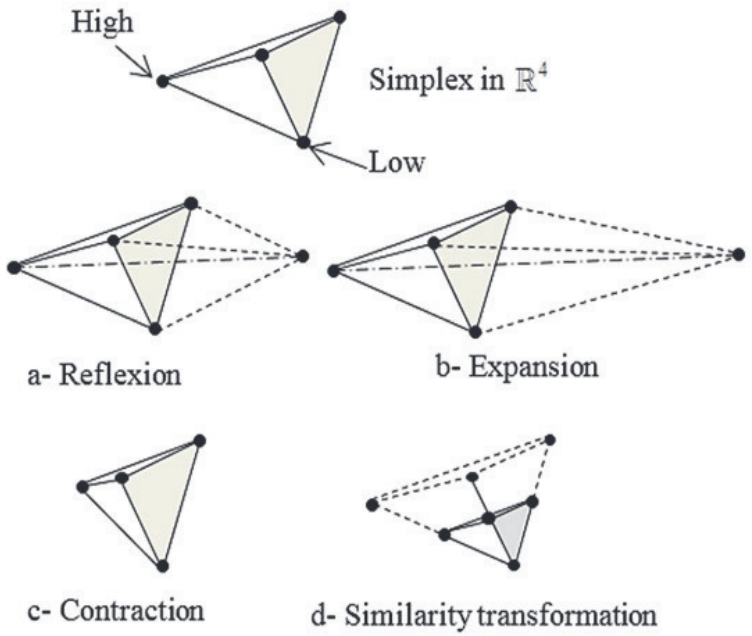

Figure 8. Function level sets and application of the Nelder-Mead simplex algorithm [15].

2.3.2. Gradient-based techniques

The gradient-based algorithms converge rapidly around the final solution; therefore, they offer a tremendous advantage in terms of speed. In addition to OF values, these methods use gradient information (first-order) and Hessian (second-order). However, their implementation is not straightforward because the derivative of the OF must be calculated first. Furthermore, they can quickly reach a local minimum depending on the initial trial point, which makes them user dependent. This is particularly relevant for multi-objective optimization problems, where the objective function depends on several variables because this type of problem has several local minimums [16].

Among the widely known gradient-based methods, *Newton´s* method (second order) and *steepest descent* method (first-order). Several modifications were made to improve these methods. One of the most popular methods is the Levenberg-Marquardt method, which modifies Newton´s method. A fundamental issue regarding optimization using second-order gradient-based optimization methods, such as this one, is the initial guess for the set of parameters; if it is not carefully chosen, the iterative method can lead to convergence difficulties [11]. To address this issue, a first-order method can be used to determine the starting point and then cascade with the second-order method [17].

2.3.3. Evolutionary methods

Evolutionary algorithms (EA) are inspired by nature and have demonstrated their capability to obtain good solutions in complex problems. Among their advantages, we can mention the lower possibility of falling into a local minimum, computational parallelization, and ease of assessment because only the objective function information is needed, and their ability to search in a broad space owing to its statistical operations [18]. Nevertheless, these algorithms are known for the significant computational effort required to converge. Some popular EAs include genetic, particle swarm, immune, artificial bee colony, and differential evolution algorithms [19].

Let us select as an exemplifying EA: the logic is inspired by the genetic evolution that considers that the next generation (solution) is better than the previous one. This is achieved by passing the best of the current iterations to the next iteration and combining them until the best solution is reached. Sometimes, a small random variation is introduced (mutation), which accounts for a combination of a discarded value that, in combination with a current value, may provide a good fit. To perform this operation properly, an operator is required to transform the potential solution into a binary state [20].

2.4. Objective function

Optimization problems require an objective function (OF), which can be considered a measurement of the optimization performance. It should be able to "guide" the optimization problem to the final solution [21]. For material parameter identification, an objective function should lead to a parameter set such that these parameters accurately represent material behavior. Moreover, OF should be continuous and smooth when gradient-based optimization algorithms are used, whereas other algorithms such as evolutionary methods and artificial intelligence can handle noncontinuous functions. In order to obtain reliable results from the parameter identification procedure, the objective function should fulfill the following requirements [22]:

- Errors in the experimental data should not be accounted for by the OF. This can be achieved by deleting experimental points of poor quality.
- For all points in a curve, each point should have an equal opportunity to be optimized, regardless of the number of points per curve.
- If multi objectives are required, OG should deal with each one and provide equal opportunity to be optimized.
- Different units or scales should not affect performance. Therefore, it is recommended to transform it into a dimensionless scale.
- Continuity must be achieved to allow progressive evaluation during the process. Therefore, an integer or discrete function should be avoided unless the nature of the problem requires it.

- The process should be independent of the user; therefore, weighting factors must be avoided, or an automatic assignment procedure must be provided.

Many feasible solutions can exist when solving a problem, some of which are better than others. When the problem involves few design variables, it could be effortless to assess which solution is better; however, when several variables are involved or the problem is multi-objective, this assessment becomes complex. For this reason, we must have a criterion that quantifies each feasible design; this is accomplished by the objective function, which serves as a criterion for determining the solution performance.

The optimization target can be minimizations (e.g., component weight, displacement, cost among others) or maximization (e.g., fatigue resistance, stiffness, production rate, eigenfrequencies, among others). This allows us to handle multiple objectives through the same optimization, such as maximizing the component stiffness, while reducing the weight. When multiple sub-objectives are pursued, it is common to have both minimization and maximization targets. In these cases, maximization can be transformed into minimization by taking the negative value of the function, as Equation 2:

$$f(\text{maximum}) = -f(\text{minimum}) \qquad \textit{Equation 2}$$

2.5. Design variables and constraints.

The design variables are values that can be changed to optimize the solution; the variation is typically performed between the upper and lower limits for each variable. These values delimitate the quest region (also known as the design space) for each problem and guarantee that the obtained result is meaningful; therefore, limits are determined by the physics of the problem. For instance, if a fraction in a blend is a design variable, its value can range from 0 to 100 %, and proper inequality can ensure the correct physical setup.

On the other hand, the constraints are binding the design variables among them or simply establishing a boundary for a design variable such that multiple conditions can be applied simultaneously to the design space. These mathematical relationships are expressed as inequalities that, for instance, define an upper limit for mass or stress. After applying the corresponding constraint, the design space is transformed into a feasible region, as Figure 9, where the dashed lines represent the constraints, and points inside the region are feasible solutions because they meet all conditions.

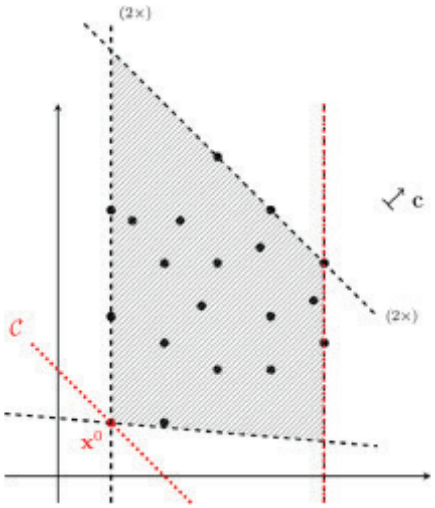

Figure 9. Feasible region delimited by constrains [23].

Reprinted with permission from Elsevier.

2.6. Parameter identification

Material parameter identification is an ill-posed problem, and small errors in input data can lead to a lack of accuracy [24]. This means that the solution achieved involves some amount of uncertainty; therefore, an evaluation of the error must be provided in order to offer a clear understanding of the limitations. The process of identifying a set of material parameters for a constitutive equation is normally performed using an inverse approach, where the objective function quantifies the gap between the experimental observations and the calculated values, which is then minimized through an optimization procedure [25].

2.6.1. Problem statement

Let U denote the observed values in the experiment (for instance, a stress field), and let $\boldsymbol{e}$ denote the given data from *U*. Furthermore, to account for the possibility that incomplete data from the experiment are available, we introduce the operator *M,* mapping $\boldsymbol{e}$ in the measurements field *U*. Then, the problem can be stated as follows:

$$\text{Find } M = \boldsymbol{e} \text{ for a given } \boldsymbol{e} \in U \qquad \textit{Equation 3}$$

The objective is to solve the problem stated in Equation 3 in a backward calculation. Nevertheless, it is well known that this problem does not have a direct solution [26];

therefore, the backward calculation is replaced by an optimization strategy, minimizing the gap between observation operator *M* and experimental observation e.

For material parameter identification, this is performed as a reverse engineering problem, that is, a calculated response is fitted to its corresponding experiment. Let us consider the stress stain response as an example, as Figure 10, where we show the experimental measurements and the calculated (numerically) curves. The reverse engineering problem consists of a gap reduction between the two curves. To achieve this, a function that calculates the distance must be defined, which can be considered as the objective function; therefore, the inverse problem can be solved by minimizing the function value.

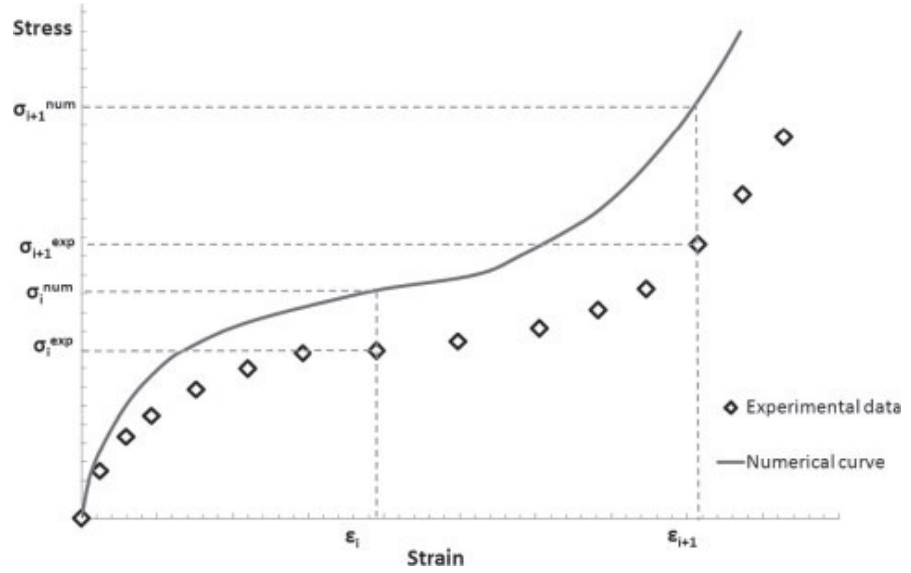

Figure 10. Experimental vs. calculated stress [17].

Reprinted with permission from Elsevier.

2.6.2. Inverse problem posedness

Once the inverse problem is stated, its posedness must be considered, that is, the solution must exist, be unique, and stable (continuous). Because different solutions can lead to similar outputs for the same inverse problem, identification or model calibration using reverse engineering is typically considered ill-posed [27]. For instance, two different sets of parameters can produce the same stress-strain response in a constitutive equation.

Posedness has been studied for many types of applications, and material parameters are well known. For example, Shrot and Baker [28] studied the uniqueness of the Johnson-Cook (J-C) model; they found that the prediction of cutting forces and chip shape for

different sets of parameters are indistinguishable; therefore, it is not possible to completely eliminate the non-uniqueness. In the best cases, uniqueness has been achieved partially for some parameters; for instance, Seupel et al. [29] were able to achieve it when using the Gurson-Tvergaard-Needleman model (GTN) for the initial crack length and critical porosity. This conclusion was supported by the findings of Zhang et al. investigation [30]; in their work, it was shown that low-sensitivity parameters can be accurately identified when a subset of parameters that exhibits a low interaction effect is chosen, and this mitigates the non-uniqueness of those parameters.

The final topic related to posedness is the stability of the solution values, which is also known as sensitivity analysis and refers to the ability of the optimal solution to produce stable values when small perturbations are introduced in the experimental data. For instance, Mahnker and Stein [26] investigated the stability of numerical results for material parameter identification using the eigenvalues of the Hessian of the least-squares functional. It is also possible to study this sensitivity by introducing a small perturbation in a finite element model [31] or artificially using stochastic methods [32].

3. MATERIALS AND METHODS

In this section, the material used to conduct the investigations is defined, starting with its chemical composition, followed by the test method conditions, and finally, the flow curves obtained.

3.1. Material description:

38MnVS6 steel was selected for this study, and its chemical composition, determined by spectrometry, is shown in Table 1. This steel is widely used in hot forging applications to produce crankshafts and connecting roads, among other automotive components. The main benefit of these types of steels is cost savings, because one of their important strength increases is achieved by micro alloy additions (e.g., Al, Nb, Ti, and V) without quenching and tempering [33].

Table 1. Chemical composition of 38MnVS6 steel (mt. % and Fe to balance).

C	Si	Mn	P	S	Cr	Ni	Mo	Cu	Al
0.522	0.260	0.837	0.010	0.025	0.142	0.062	0.018	0.155	0.025

38MnVS6 steel has been widely investigated in the literature; for instance, Gu et. al. [34] modeled the dynamic recrystallization (DRX) behavior based on a hot compression test and found that DRX increases when the temperature and strain rate increase. Nalawade et al. [35] investigated its behavior during the hot rolling processes, during the initial passes in a blooming mill, as a function of three different pass schedules, roll groove depth, collar taper angle and corner radius. Furthermore, Niu et al. [36] studied the fatigue and oxidation characteristics of 38MnVS6 and 42CrMo4 and found that the latter possessed better fatigue resistance and lower oxidation at high temperatures. Recently, Ercayhan and Saklakoglu [37] investigated the effects of the forging temperature and cooling rate on the metallurgical and mechanical properties. They found that, for this steel, the amount of ferrite increased when the forging temperature decreased, which improved the toughness.

3.2. Experimental conditions:

Considering the compressive nature of the hot forming operation, the classical and well-established uniaxial tension test cannot capture the material's behavior. Therefore, the hot compression test is needed since it represents the compressive nature of the process.

Moreover, based on what is stablished in Equation 1, when it comes to implementation into finite element simulation, we need to keep the stress as a function of strain, thus, in order to achieve that, the stain rate and the temperature should be constant during the test. The compression test allows for high speed (consequently high strain rates), even though it has the inconvenient of the friction between the same and the compression anvils.an addition drawback is the lack of standard for this test, which makes difficult result homologation and comparison among testing laboratories and even among different equipment.

This study employed 38MnVS6 steel as the material, and its chemical composition was determined by spectrometry, as detailed in Table 1. Plastic flow stress profiles were acquired via cylindrical compression testing. Test specimens measuring 18 mm in height and 10 mm in diameter were meticulously machined and polished. The experiment employed a Bähr MDS 830 thermomechanical simulator from BÄHR Thermoanalyse GmbH (Hüllhorst, Germany). This apparatus integrates an inductor heater and vacuum chamber. The testing protocol involved heating the specimen at a rate of 2.5 K/s until it reached the desired deformation temperature. Subsequently, a 5-minute hold period was provided prior to initiating deformation, as illustrated in Figure 11. To manage and correct the temperature deviations during testing and post-processing, an S-type thermocouple was affixed to the center of the outer cylindrical surface of the specimen. The resultant sample attained a final height of 6 mm, corresponding to a logarithmic (true) strain of roughly one (100%). Deformation occurred at temperatures of 900, 1000, 1100, and 1200 °C, coupled with deformation strain rates of 0.1, 1, 15, and 30 s^{-1}. The flow stress curves were meticulously adjusted for temperature variations, friction, and strain-rate discrepancies.

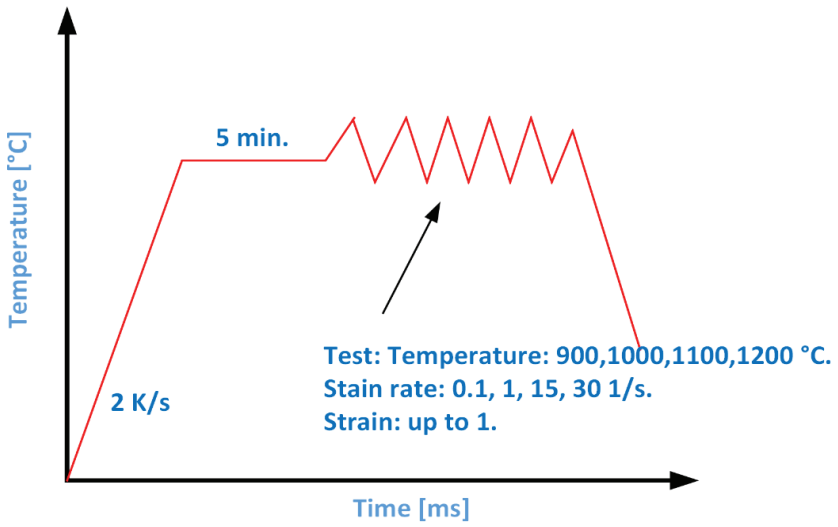

Figure 11. Experimental description of the hot compression test.

3.3.Experimental apparatus and specimens

As it was shortly introduced in the previous section, the experimental apparatus used to carry out these experiments was the thermomechanical simulator MDS 830 from BÄHR Thermoanalyse (now TA Instruments [38]), located at the TU Bergakademie Freiberg (Germany), Institute for Metal Forming. This apparatus has 250 KN force capacity, capable of performing uniaxial tension, compression, and torsion (by changing grippers). As for the compression test, it can achieve strain rates going from 0.01 to 100 s^{-1} while providing energy to achieve up to 1400°C. These capabilities are enough to cover the wide range of metal forming operation.

This equipment is enclosed by a vacuum chamber, preventing the oxidation of the sample (carbon react with oxygen from the air), which eliminates the environmental variability. Inside the chamber, the there are several components, as can be seen in Figure 12 (a), including the grippers, an inductor coil, anvils, an actuator, and sensors. In Figure 12 (b), a detailed view of the specimen mounted on the lower anvil is shown. The flow as follows: i) the thermocouple is welded to the cylindrical surface the specimen, ii) the specimen is mounted on the lower anvil, iii) the chamber is closed and vacuum condition is achieved, iv) the inductor heats up the specimen and give the holding time, v) the piston accelerate to achieve appropriate velocity and reduce it while compressing.

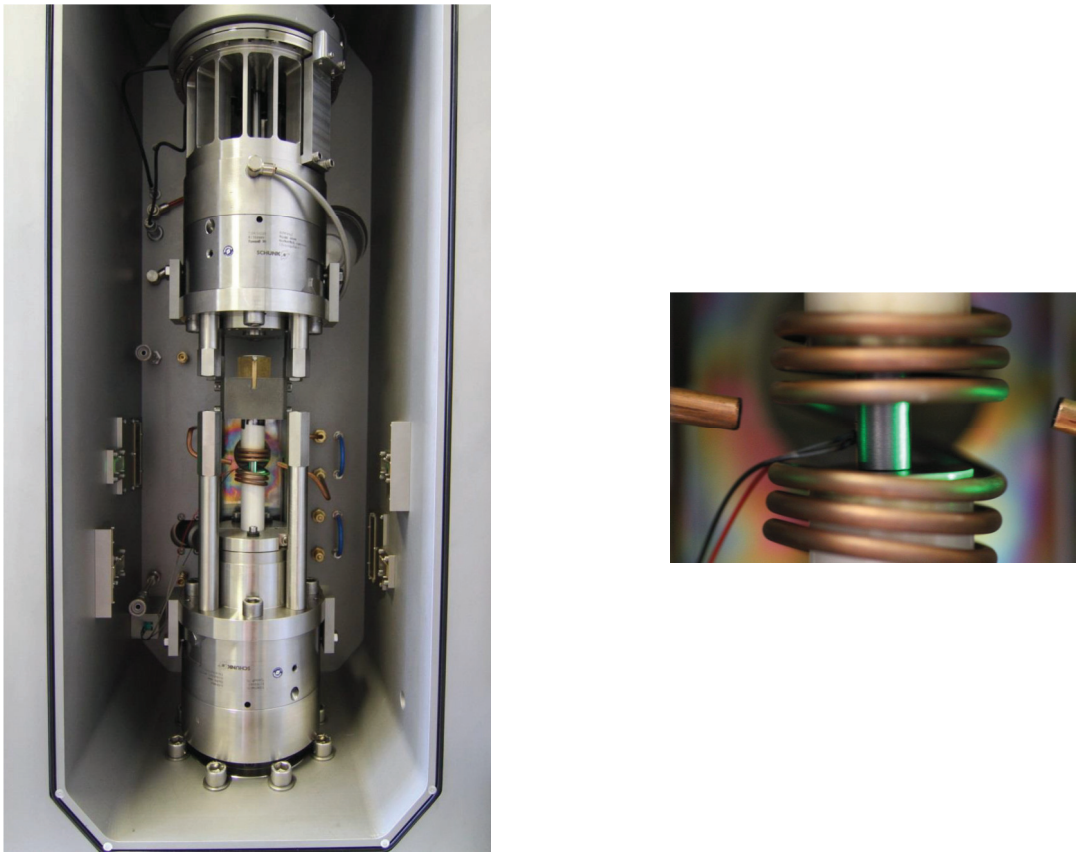

(a) (b)

Figure 12. Thermomechanical simulator MDS 830 [39].

The thermocouple has two purposes: first, it is used as feedback for the proportional-integrate-derivative (PID) control loop, ensuring the heating ration is maintained and held during the homogenization time. Once the test starts, the duration is such small that there is not chance to control temperature, however, the thermocouple provides the measurements to estimate if the specimen is kept within an acceptable range; there are two options: the temperature increases due to the mechanical work or, it decreases due to the radiation lost.

The strain rate is maintained constant by varying the velocity profile during the compression based on Equation 4, where v is the instant velocity and h is the specimen's height at the same time. Therefore, the lower the height, the lower the compression velocity is needed to maintain a constant strain rate. The velocity profile used is shown in Figure 13 for 15 and 30 s^{-1}; we can see that the velocity is reduced while the test time progress (anvil moves downwards and compress the sample). Temperature is also a central aspect for hot compression test, the experimental values measured during the test are given in the Appendix C. There we can see some small variation for the temperature, this is cause to the loss due to radiation, and some increase due to conversion of deformation energy into thermal energy.

$$\dot{\varepsilon} = \frac{v}{h} \qquad \text{Equation 4}$$

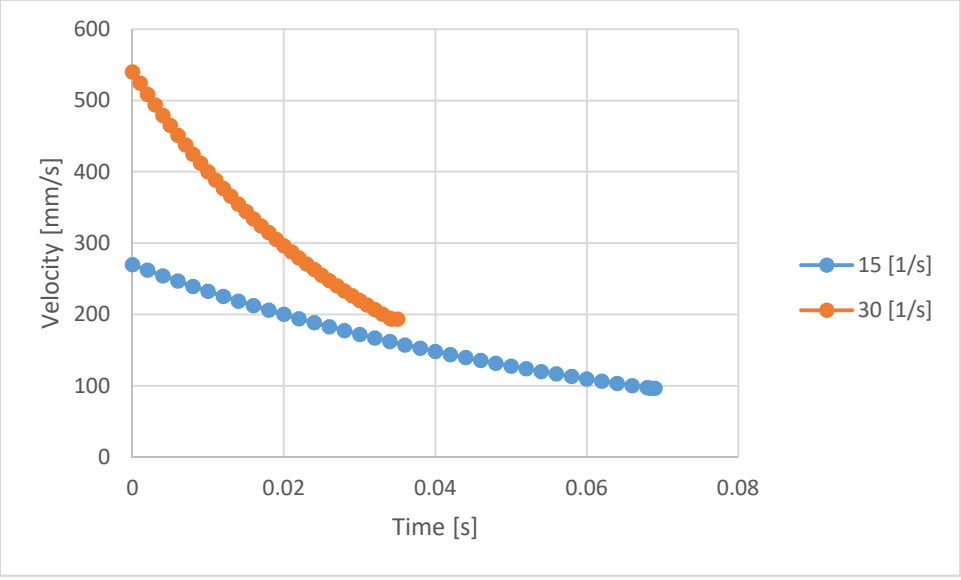

Figure 13. Velocity profile for compression.

3.4. Experiment results

The flow curves obtained from the experiments described above are shown in Figure 14. The results are arranged in four sub charts corresponding to each temperature, and different strain rates are given for each temperature. Three repetitions were conducted for each condition, and the average is shown. In these results, the effect explained above can be observed: the higher the temperature, the lower the flow stress; therefore, less energy is needed to achieve the same amount of deformation. Similarly, for each temperature, it is shown that the higher the strain rate, the higher the flow stress, which is due to viscous effects; therefore, more energy needs to be applied to deform the material when higher strain rates are used.

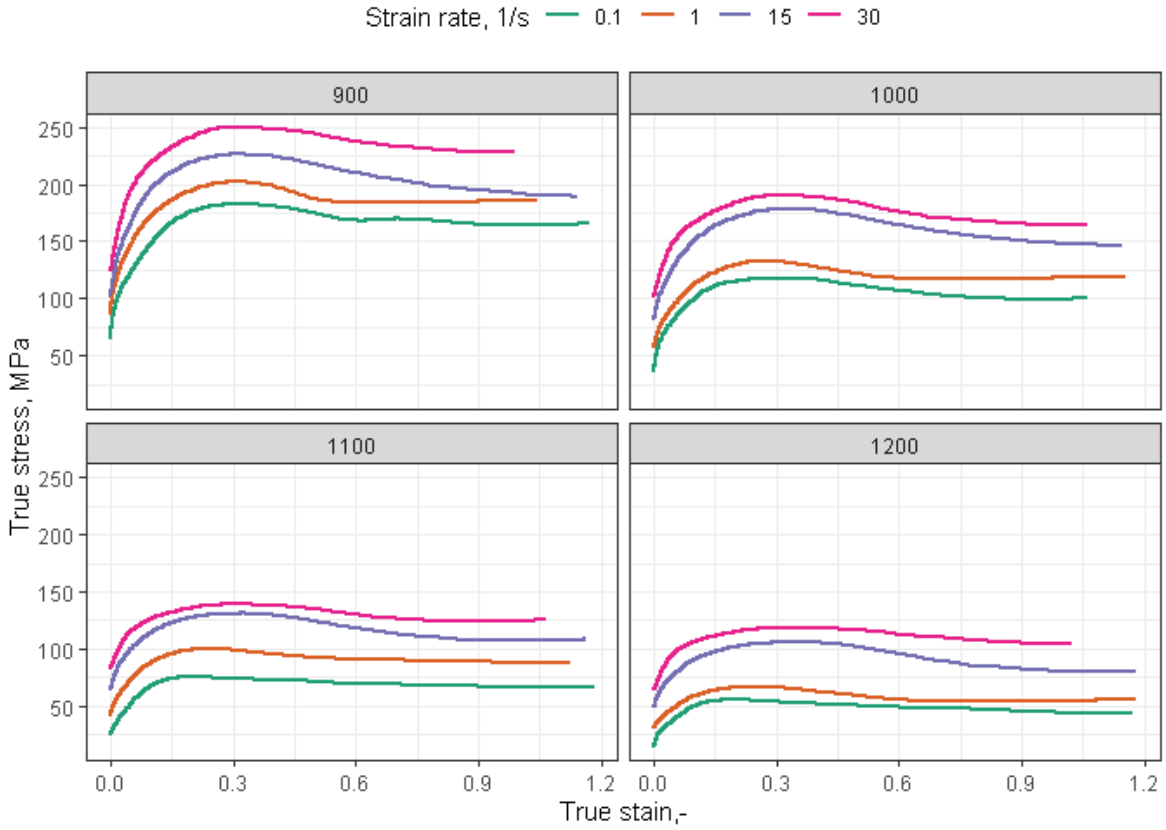

Figure 14. Experimental flow curve obtained for 38MnVS6 steel.

3.5. Activation energy

The Zener-Hollomon parameter (Z) in combination with the Arrhenius equation was used to determine the activation energy (Q), as follows:

$$Z = \dot{\varepsilon} * e^{\left(\frac{Q}{R*T}\right)} = f(\sigma) \quad \textit{Equation 5}$$

Where $\dot{\varepsilon}$ is the strain rate, R is the universal constant of gases, T is the deformation temperature, whereas $f(\sigma)$ is a stress function related to Z and the most commonly used function are described in Equation 6 to Equation 8 [40].

$$f(\sigma) = A_1\sigma^{n_1} \quad \textit{Equation 6}$$

$$f(\sigma) = A_2 * \exp(\beta\sigma) \quad \textit{Equation 7}$$

$$f(\sigma) = A_3[\sinh(\alpha\sigma)]^n \quad \textit{Equation 8}$$

where $A_1, A_2, A_3, n_1, n, \alpha, \beta$ are temperature-independent material constants that can be determined by applying multiple regression. In general, the power law described by Equation 6 is suitable for low-stress values. Conversely, the exponential law shown in Equation 7 is only suitable for high stresses. Finally, the hyperbolic sine given by Equation 8 can be used for a wide range of temperatures and strain rates. The material constants are related by the following equation [41]:

$$\alpha = \frac{\beta}{n_1} \quad \textit{Equation 9}$$

Now, by combining the Equation 5 and Equation 6 we obtain:}

$$\dot{\varepsilon} * e^{\left(\frac{Q}{R*T}\right)} = A_1\sigma^{n_1} \quad \textit{Equation 10}$$

Rearranging and taking the natural logarithm.

$$\ln\dot{\varepsilon} = \ln A_1 + n_1 \ln\sigma - \frac{Q}{R*T} \quad \textit{Equation 11}$$

At a constant temperature, Q remains constant and therefore, it is possible to obtain n_1 from the applying regression. In this case, the highest strain value is considered, i.e., $\varepsilon = 1$. Because four different strain rates were considered during the experiment executions, a plot of four points per temperature is shown in Figure 15, where dots represent the experimental point and dashed lines represent their regression. The results for each temperature are listed in Table 2, and the regression coefficient is given for each temperature. As can be seen, the regression offers good approximation relevance; nevertheless, n_1 is not constant and increases with temperature. Its average is considered in this study, although it shows a high standard deviation of approximately 30 % of the average.

Table 2. The results of the linear regression used to determine n_1.

T [K]	n_1	R^2
1173	0.0471	0.823
1273	0.0849	0.991
1373	0.1025	0.979
1473	0.1430	0.956
Average	0.0944	
Std. Dev.	0.0398	

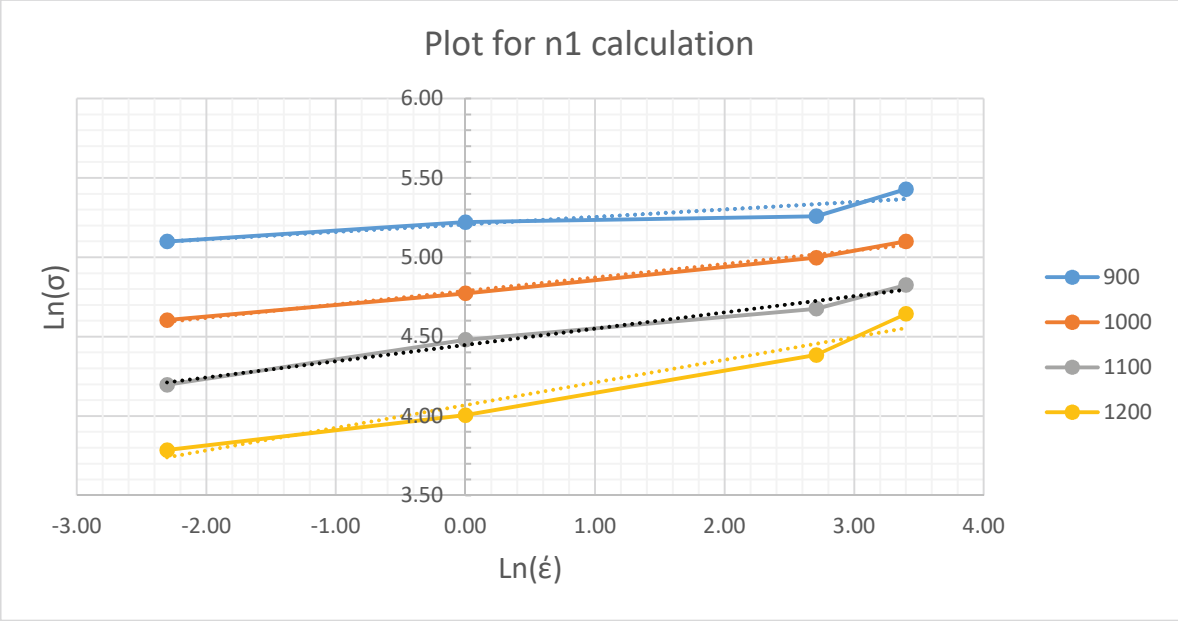

Figure 15. Regression plot for n_1 calculation.

Similarly, by considering Equation 5 and Equation 7, at a constant temperature for each strain rate value, we can obtain Figure 16, from these regressions a β coefficient for each

temperature is obtained, and the average is considered as shown in Table 3 alongside the regression coefficient.. Notably, in this case, the standard deviation was only 9 % of the average value.

$$\ln \dot{\varepsilon} = \ln A_2 + \beta\sigma - \frac{Q}{R * T}$$ *Equation 12*

It is interesting to note that both n_1 and β have regression coefficients that increase with temperature; however, in the case of n_1, this shows a greater variation based on its standard deviation. The approach of taking the average is a simplified method for determining the temperature-independent material constant over a wide range of temperatures and strain rates.

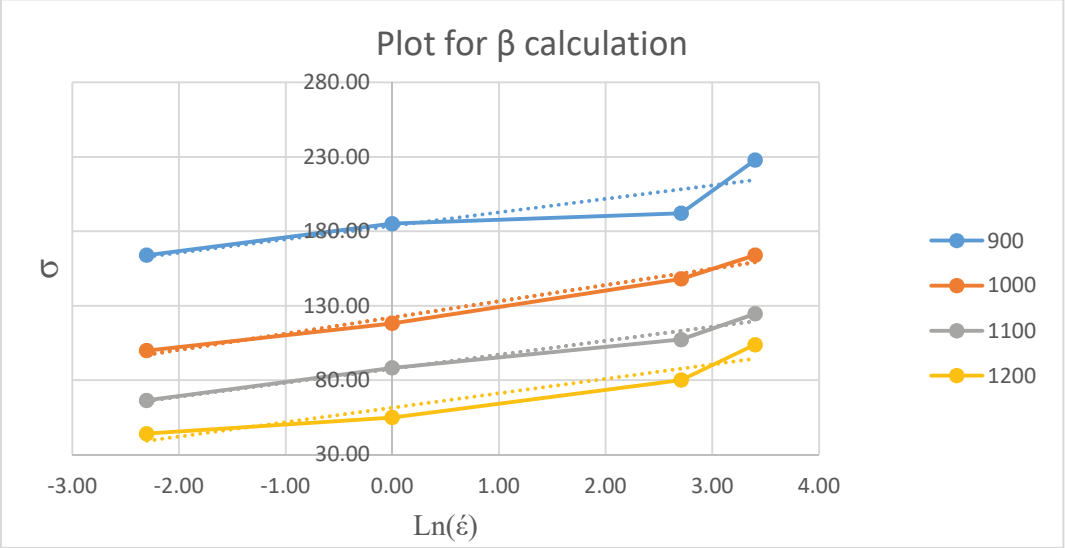

Figure 16. Regression plot for β calculation.

Table 3. Results of linear regression to determine β.

T [K]	β	R^2
1173	9.02	0.792
1273	10.90	0.976
1373	9.39	0.968
1473	9.7	0.901
Average	9.75	
Std. Dev.	0.81	

Equation 8 can be used for a wide range of stresses and strains, and furthermore, based on the intended application of hot forging, where the strains can reach large values, as can be seen in Figure 14, and combining this with Equation 5:

$$\dot{\varepsilon} * e^{\left(\frac{Q}{R*T}\right)} = A_3[\sinh(\alpha\sigma)]^n \qquad \textit{Equation 13}$$

Taking the logarithm of both sides of Equation 13,

$$\ln \dot{\varepsilon} = \ln A - \frac{Q}{RT} + \mathrm{n} * \ln[\sinh(\alpha\sigma)] \qquad \textit{Equation 14}$$

It can be inferred from Equation 14 that a at a particular strain value, the experimental data yield to a parallel and linear relationship between $\sinh(\alpha\sigma)$ and $\ln \dot{\varepsilon}$ for a given temperature value. And now, using the Equation 9, as well as the values determines for n_1 and β, we can calculate α; its results and standard deviation are shown in Table 4. It is noteworthy that the standard deviation reached 43 % of the average value, which might be due to the high variations observed for n_1 value.

Table 4. Calculated values for α.

T [K]	n_1	β	α
1173	0.0471	9.02	0.00522
1273	0.0849	10.90	0.00779
1373	0.1025	9.39	0.01092
1473	0.1430	9.7	0.01474
Aver	0.0944	9.75	0.00967
Std. Dev.	0.0398	0.81	0.00411

The activation energy can be expressed as the slope of the different plots by taking the partial derivative as follows:

$$Q = R\left\{\frac{\partial \ln \dot{\varepsilon}}{\partial \ln[\sinh(\alpha\sigma)]}\right\}_T \left\{\frac{\partial \ln[\sinh(\alpha\sigma)]}{\partial(1/T)}\right\}_{\dot{\varepsilon}} = R * N * K \qquad \textit{Equation 15}$$

To obtain the terms *N* and *K*, two plots were required, as shown in Figure 17 and Figure 18, respectively. As before, the solid lines represent the experimental points, and the dashed lines are obtained by means of linear regressions. A summary is given in Table 5: the values of *N* and *K* are shown, as well as their averages and standard deviations, from which it can be observed that the deviation achieves 14 % and 12 % of the average value, respectively. These deviation values are significantly high when compared with the average value, indicating that the variations across the temperature and strain rate are significant. Nevertheless, when we look at the regression coefficient for each temperature and strain rate value, we observe a good correlation value (above 94 %, except at 1173 K).

Table 5. Summary of activation energy calculated for each temperature and strain rate.

T [K]	n1	β	α	1/n	n	S.R.	k	Q
1173	0.0471	9.02	0.00522	0.0918	10.89	0.1	9559.00	865.72
1273	0.0849	10.90	0.00779	0.1250	8.00	1	9261.00	615.97
1373	0.1025	9.39	0.01092	0.1286	7.78	15	7529.00	486.75
1473	0.1430	9.7	0.01474	0.1639	6.10	30	7720.00	391.61
Aver	0.0944	9.75	0.00967		8.1926		8517.25	590.01
Std Dev	0.0398	0.81	0.00411		1.9898		1040.94	205.52

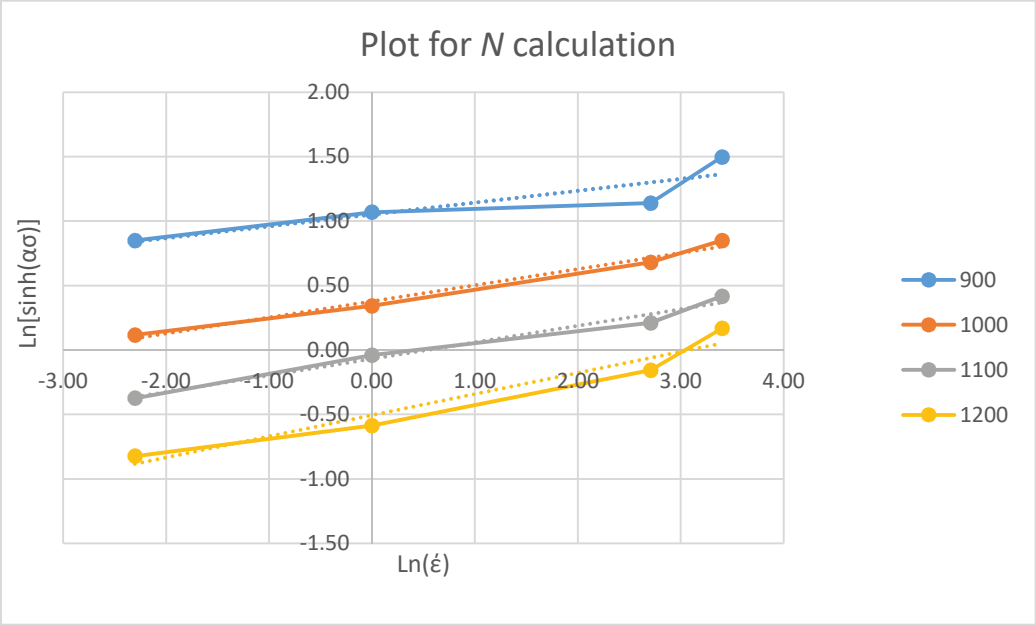

Figure 17. Linear regression to obtain N.

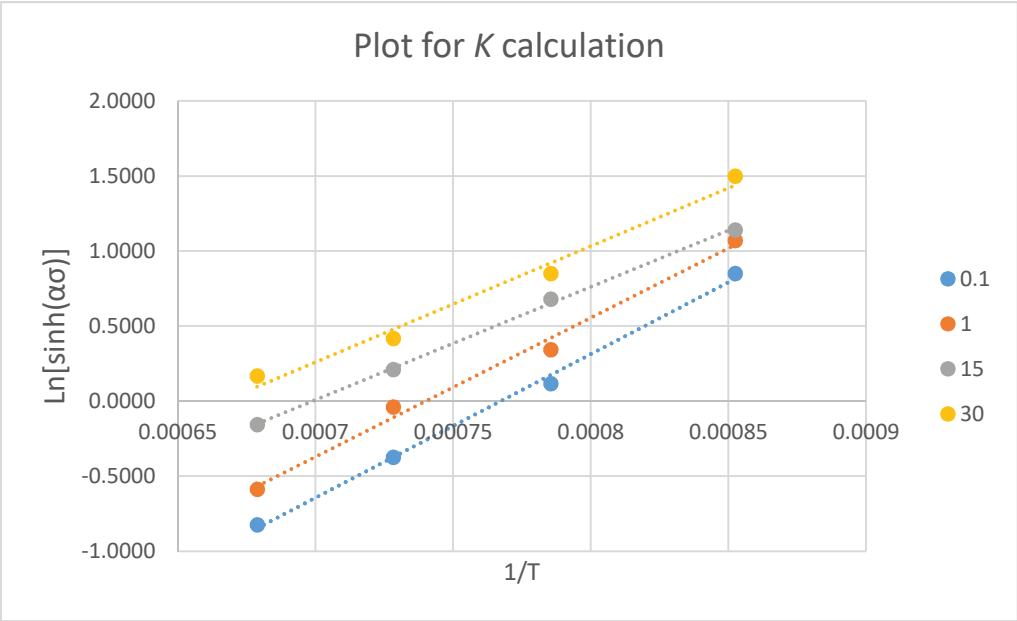

Figure 18. Linear regression to obtain K.

A similar condition can be observed for the activation energy Q, where the deviation was 35 % of the average value. Certainly, it is possible to obtain additional values of Q, as can be inferred from Equation 15, by combining each temperature with different strain rate values. When 16 combinations are done, Q is calculated as the average value of 580 KJ/mol, which represents a drop of 2 % in the average obtained previously; however, the standard deviation was reduced from 205 to 137 KJ/mol. A good approach to verify the relationship described by the Z parameter is to combine Equation 5 and Equation 8, which returns the following expression:

$$Z = A_3[\sinh(\alpha\sigma)]^n \qquad \textit{Equation 16}$$

When the logarithm is taken from both sides of Equation 16, a linear plot must appear, as shown in Figure 19, where a regression coefficient of $R^2 = 0.975$ is obtained, which confirms that the experimental results satisfy this mathematical relationship.

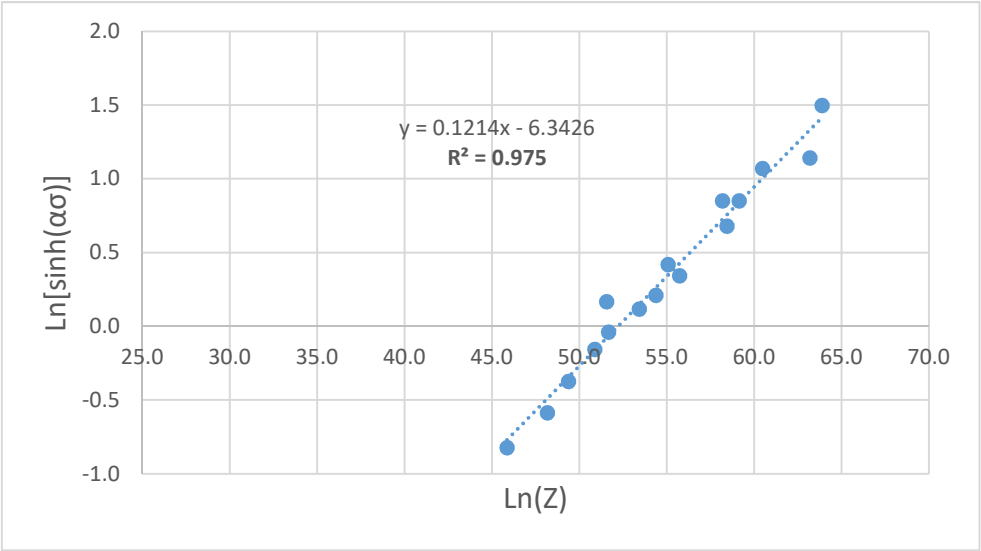

Figure 19. Logarithms of Equation 16 confirming mathematical relationship.

This reduces the calculated standard deviation. Moreover, the values here shown correspond to the stress exhibited at $\varepsilon = 1$, therefore, it makes sense to study the behavior at the peak stress value, since as describe in the previous chapter, after the peak value, there is a change from DRV to DRX. We consider a straightforward method to verify these relationships by combining Equation 5 and Equation 8, as shown in Equation 16. A linear equation must be obtained by taking the natural logarithm of both sides of the latter equation.

4. PARAMETER IDENTIFICATION FOR HOT FORGING APPLICATIONS

Based on the experimental results shown in Chapter 3, as well as the classical approach to modeling this material´s behavior, we can conclude that the behavior is more complex at elevated temperatures than at room temperature. This is due to the interaction between temperature, strain rate, and strain, and their effects on the stress response, which leads to the previously described stage during deformation: work hardening, softening, steady state, accompanied by DRX and DRV. Therefore, a more sophisticated approach is required to properly model material response. The approach considered in this chapter is to take a constitutive equation suitable to describe the phenomenon, and then, by applying an optimization strategy, the parameters are identified.

4.1. Constitutive equations

During Finite Element Analysis, a constitutive equation was used to compute the stress based on the strain (among other variables). A constitutive equation can be described as a mathematical relationship that correlates a dependent variable with a set of "independent" variables [42]. Quotes were used because the independent variable may depend on other variables or process parameters. There are two classical types of constitutive equations [43]: phenomenological models and physically based models. Furthermore, owing to the significant progress in artificial intelligence and machine learning algorithms, a new category has recently appeared: models based on neuronal networks [44]. This study does not consider the latter category.

A perfect constitutive equation should involve a limited set of material characteristics, the identification of which requires only a minimal number of experiments. Simultaneously, it should provide an accurate simulation of phenomena across a broad range of strains, strain rates, and temperatures [45].

4.1.1. Physically based equations

These equations consider the physical characteristics of a material. These principles encompass aspects related to thermodynamics, thermally driven motion of dislocations, and mechanics of slip. In contrast to purely observational descriptions, these models provide a precise characterization of the material behavior across a broad spectrum of loading conditions by relying on certain physical assumptions and a greater number of material constants. Therefore, their parameters always have physical meaning, describing the attributes or properties of a material. For instance, Zamani et al. [46] proposed a model based on the dislocation density, assuming the flow stress can be separated in two major components, as follows:

$$\sigma = \sigma^* + \sigma_G$$ *Equation 17*

where σ^* represents the stress required to overcome short-range obstacles through thermal activation, while σ_G denotes the stress contribution arising from long-range interactions within the dislocation substructure. The short-range stress component is expressed as follows:

$$\sigma^* = \tau G \left\{ 1 - \left[\frac{k * T}{\Delta f * G * b^3} \ln\left(\frac{\dot{\varepsilon}_{ref}}{\dot{\varepsilon}_p} \right) \right]^{\frac{1}{q}} \right\}^{\frac{1}{p}}$$ *Equation 18*

Where $\tau, \Delta f$ are optimization factors, G is the shear modulus. K is the Boltzmann constant, T is the temperature, b is the Burgers vector, $\dot{\varepsilon}_{ref}$ is the reference strain rate, $\dot{\varepsilon}_p$ is the applied strain rate, whereas p and q characterize the shape of the energy barriers and have the values of $0 < p \leq 1$ and $0 < q \leq 2$.

Thermally induced stress typically pertains to the resistance encountered from short-distance obstacles, including the interaction of closely positioned dislocations (known as intersection slip), the Peierls stress in the case of BCC crystal structures, and the restraining influence of solute atoms, whether they are interstitial or substitutional; these effects are well explained by Yuan et al., [47]. This approach has been successfully used in finite element models [48] and in metal cutting analysis [49].

4.1.2. Phenomenologically based equations

Phenomenological constitutive models provide a flow stress definition based on empirical observations utilizing mathematical functions. Nevertheless, they lack a solid physical foundation that aligns precisely with experimental findings. However, they have a noteworthy ability to minimize the number of material constants and facilitate straightforward calibration. Furthermore, owing to their empirical nature, these models are typically limited in their application, mainly within specific strain rates and temperature ranges, and exhibit restricted adaptability for specific materials.

Phenomenological models are widely used in metal-forming applications and several models are available. For instance, Khan and Huang [50] proposed a viscoplastic model that can predict aluminum behavior under large strain values; however, they only considered low strain rates (10^{-5}-10^{-4} 1/s). In addition, one of the most widely used

phenomenological models (in the author´s opinion, the most widely used) was proposed by Johnson and Cook (J-C) [51], as shown in *Equation 19*.

$$\sigma = \left(\sigma_o + B\varepsilon_p^n\right) * \left(1 + C\ln\frac{\dot{\varepsilon}}{\dot{\varepsilon}_r}\right) * \left(1 + \frac{T - T_r}{T_m - T_r}\right)^q \qquad \textit{Equation 19}$$

Where B and n are hardening coefficient and exponent, respectively, σ_o is the reference stress, C is viscous coefficient., q is the thermal exponent, T is the temperature, $\dot{\varepsilon}$ and $\dot{\varepsilon}_r$ are the strain rate and its reference value, respectively. Originally, the J-C model was proposed to model high-velocity impact problems, and later, owing to its simplicity, it has been extensively used in different fields, such as metal cutting [52]. Zhe et al. [53] used the J-C model to predict the plastic strain in aluminum 6016-T6 alloy sheets under a low dynamic strain rate (up to 100 s^{-1}); however, because the J-C model is not intended to be used under a low strain rate, they implement4ed a quadratic function to improve the strain rate sensitivity of the constant C. Another contribution to improving the softening prediction above 400°C for the J-C model was performed by Priest et al., [54]. This was achieved by making the parameters C and q temperature-dependent; the intention was to give them mathematically the ability to capture the nonlinearity due to the temperature.

One of the least-known constitutive models for integration into finite element codes is the Hensel-Spittel (H-S) model [55]. The mathematical expression for the H-S model is described by *Equation 20*, where temperature, strain, and strain are the phonological variables represented as before, whereas A and m_i are the parameters to be identified.

$$e^{m_1 T}\varepsilon^{m_2}\dot{\varepsilon}^{m_3}\left(e^{m_4/\varepsilon}\right)(1+\varepsilon)^{m_5 T} * e^{m_6\varepsilon} \qquad \textit{Equation 20}$$

The H-S model has a significant advantage because it considers factors individually as well as their interactions. However, this model has some shortcomings: its accuracy varies with the number of parameters considered during the identification procedure [56]. This means that not all parameters are required for every material intended to be fitted. Therefore, a common approach is to run the identification procedure by assigning a zero value to some parameters and taking the one that provides the best fit [57].

4.2. Problem statement

In this work, the J-C model, given by *Equation 19*, and the H-S model, given by *Equation 20*, are used to model the material behavior of 38MnVS6 steel, as shown in Figure 14. The

problem can be defined as the search for a set of parameters such that the calculated floe stress matches the experimental one. The topic now is how to identify a set of parameters such that the calculated value matches the experimental value. There are several methods as discussed before; however, in this work, attempts are made by using mathematical regression for the J-C model and optimization strategies for both models selected.

The next topic to consider is the assessment of the accuracy of the obtained parameters. There is a direct option when optimization is used, which consists of taking the final value of the objective function, with the lowest value representing the best fit. In this study, two measurement quantities are employed to assess the accuracy of the results, that is, the Root Mean Square Error (RMSE), which is a frequently used measure of the differences between values predicted by a model. In addition, the Average Absolute Relative Error (AAE), which is a method of measuring the performance of a predictive model, was used. The mathematical expressions are given by *Equation 21* and Equation 22 respectively.

$$RMSE = \frac{1}{M}\sum_{j=1}^{M}\sqrt{\frac{1}{N}\sum_{i=1}^{N}\left(\sigma_{exp} - \sigma_{cal}\right)^2} \qquad \textit{Equation 21}$$

$$AARE = \frac{1}{M}\sum_{j=1}^{M}\frac{1}{N}\sum_{i=1}^{N}\left|\frac{\sigma_{exp} - \sigma_{cal}}{\sigma_{exp}}\right| * 100 \qquad \textit{Equation 22}$$

In both above equations, *N* represents the number of points for each curve (discretized with 145 points), and *M* represents the number of curves to be fitted (with corresponds to the number of experimental conditions, i.e., 16 in this case). σ_{exp} represents the experimental flow stress and σ_{cal} is the flow stress calculated by the constitutive equation. RMSE is a measure of the absolute difference for each stress value at the same strain, giving the minimum distance between them. AARE is also computed through a term-by-term comparison of the relative error, thereby being an unbiased statistical parameter for measuring the predictability of a model [58].

4.3. Optimization procedure

The procedure employed in this study is commonly known as the *inverse problem*, which means that reverse engineering is utilized to determine or identify a set of parameters, such as the distance between the experimental and calculated flow stress, which is minimized. A graphical representation is shown in Figure 20, which shows the experimental points *E1* and *E2* as well as the calculated *C1* and *C2*. The task is to reduce the distance between each

pair, for example, (*E1*, *C2*), (*E2*, *C2*), … (*Ei, Ci*); therefore, a fitness operator is required to accomplish this task. The operator is commonly known as the objective function (OF), and it measures all points across the curves and under all test conditions, returning a scalar value.

The most common approach to optimization when it comes to a minimization process is the least squares method (LSM), given by *Equation 23*. This is used as an objective function and is minimized using a Genetic Algorithm (GA) in combination with a gradient-based algorithm. Finally, a starting point must be selected such that an initial calculation is accomplished, and the optimization algorithm starts to operate.

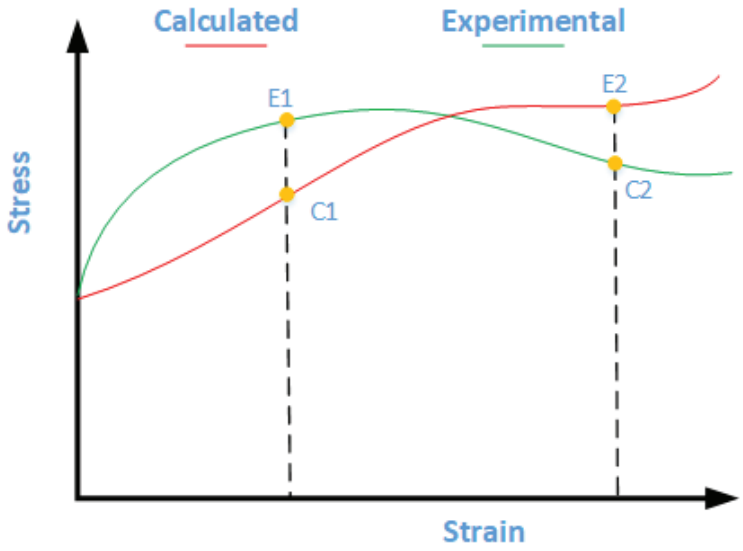

Figure 20. Graphical representation of the inverse problem.

$$OF_1 = \frac{1}{M}\sum_{j=1}^{M}\frac{1}{N}\sum_{i=1}^{N}\sqrt{\left(\frac{\sigma_{exp}-\sigma_{cal}}{\sigma_{exp}}\right)^2} \qquad \textit{Equation 23}$$

A genetic algorithm (GA) is used to identify the material parameters within the search area defined by the upper and lower bounds. After the GA converges, the search area is reduced around the solution obtained by the GA, and a gradient-based search is then performed. Because the material parameters are based on phenomenological models, there is no constraint for numerical values in the upper and lower bounds. Hence, bounds are chosen such that the search area is as large as possible to keep the model returning the feasible flow stress values. The GA is used first due to its capability avoiding local minimums,

which allows them to explore a wide search region. Once this convergence is achieved, the search area is reduced to facilitate the performance of a gradient-based algorithm.

A constitutive equation can be considered to have a unique solution when different starting points converge to the same values. To verify the uniqueness of the solution, several starting points were randomly generated within the search area, and the results were compared. The bounds and some of the starting points used for both the H-S and J-C equations are listed in Table 6Table 6. As discussed previously, for the sake of fitting, some parameters were forced to be zero for the H-S equation. This depends on each material, and for the one under investigation in this work, m_3 and m_6 were made equal to zero.

Table 6. Bounds and starting points for both the H-S and the J-C equations.

Equation	Parameter	Bounds		Starting point			
		Lower	Upper	1	2	3	4
H-S	m1	-1	0.5	-0.5	-0.01	0.01	0.1
	m2	-0.2	1.5	-0.1	0.01	0.2	0.6
	m4	-0.4	0.05	-0.25	-0.01	0.01	0.04
	m5	-1	0.02	-0.4	-0.01	0.002	0.1
	m7	-5	2	-3	-0.5	0.01	0.2
	m8	-0.01	0.01	-0.008	-0.002	0.0005	0.007
	A	10	122000	1500	6000	9000	11000
J-C	B	0	250	36.3	11.5	120	203
	n	-1	2	0.12	0.21	-0.10	1.85
	C	0	2	0.22	0.53	1.90	1.12
	q	0.01	1.5	0.73	0.11	1.20	0.01

Regarding the GA settings, an initial population of 200 individuals was established for the H-S equation. For the J-C equation, there were 100 individuals. In GA, an individual refers to a set of parameters or a chromosome, and each parameter is a gene. This setting is based on the number of parameters that need to be identified, as well as trial and error. A higher number of initial populations will involve a higher computation time; therefore, the population was adjusted to achieve an accurate result while maintaining a reasonably fast computation time. The optimization was performed employing the Altai HyperStudy® [59], which allows for different optimization algorithms, including GA and gradient-based algorithms.

4.4. Development of an objective function

Simultaneous efforts were made to develop a new objective function based on the idea that this function must be sensitive to small changes in input values. In other words, the larger the change in the OF response, the easier it is for the optimization algorithm to find a path conducting to a minimum. A new OF was proposed, inspired by the concept of “trues strain” using logarithm, and the ideas expressed by Andrade et al. [22], a second objective function is proposed in *Equation 24*. These concepts follow the idea of “true error," such as "true strain,” and apply the natural logarithmic function.

$$OF_2 = \frac{1}{M}\sum_{j=1}^{M}\frac{1}{N}\sum_{i=1}^{N}\ln\left[1+\left|\frac{\sigma_{exp}-\sigma_{cal}}{\sigma_{exp}}\right|\right] \qquad \textit{Equation 24}$$

For the sake of comparison of both function´s performance, the same starting point and bounds shown in Table 6 are used, as well as the minimization strategy described in the previous section. Therefore, the only aspect that changes is the performance, which allows us to make a fair comparison. In addition to the parameters to measure the fitness of the solution, that is, the RMSE and AARE, we can also consider the number of iterations performed before convergence is reached. Furthermore, we must consider the final value that each function achieves.

4.5. Results validation and comparison

The first aspect considered for the comparison of results is the convergence speed, that is, the number of iterations needed until the result is reached. It is expected that reaching convergence requires different iterations depending on the starting point. Moreover, because the H-S model has a higher number of parameters to be determined, convergence is expected to require more iterations. Therefore, the H-S model was used to assess the performances of both OF1 and OF2. As mentioned previously, several points were tried, and four representatives of these points are shown in Figure 21. For points 1 and 2, it was shown that OF2 reached faster convergence. For point 3, OF1 was faster than OF2, and for point 4, the number of iterations required was the same.

To compare the performance based on time taken to calculate the required iteration, all analysis were done using the laptop with 8 CPU: Intel(R) Core (TM) i7-6700HQ CPU @

2.60GHz. The time consumed and the number of iterations carried out are sown in Table 7, where the time consumed by the OF1 was used as reference to calculate the difference with OF2. For the starting points 1 and 2, we observe a time saved of 28 and 24% respectively when the OF2 is used. On the other hand, for the point 3, we observe that OF2 takes 2.6 times more than OF1; however, as it will be described later, this extra time is worth since the error result from OF2 is approximately half when compared with OF1.

Table 7. Iteration and time to converge for both functions.

Starting point	OF1		OF2		Time difference %
	time [min]	Iterations	time [min]	Iterations	
1	114	149	89	114	-28
2	72	90	58	70	-24
3	20	25	52	50	+260
4	19	25	20	25	-

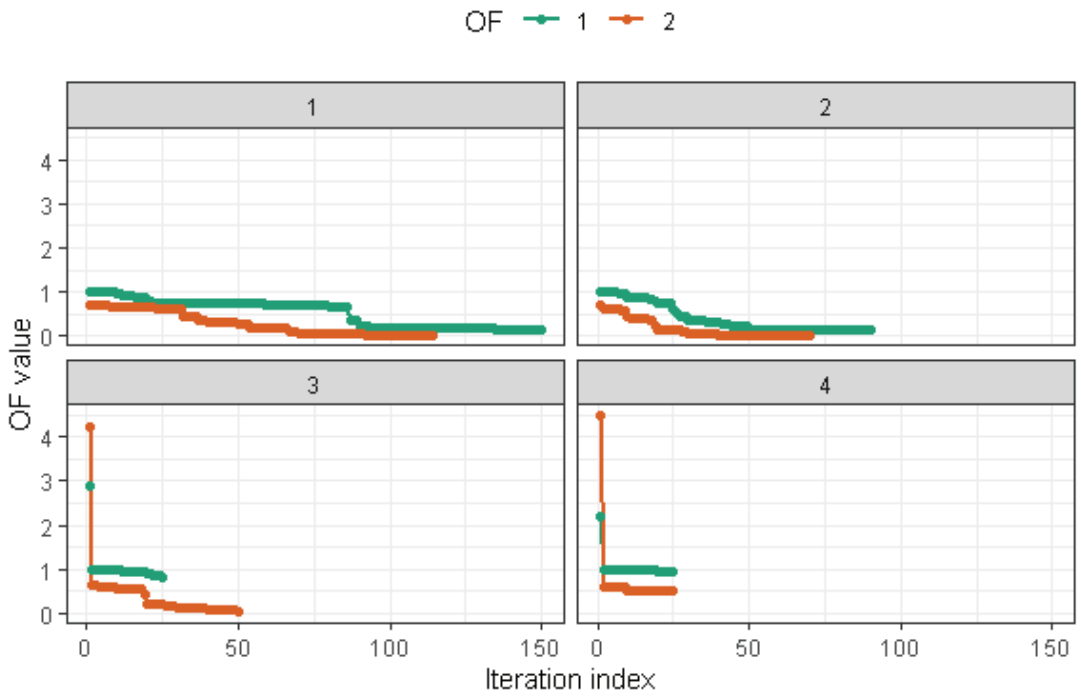

Figure 21. Results of the objective function convergence for the H-S model.

As expected, there were starting points that required few iterations to reach convergence and there were points that required several iterations (approximately six times more iterations). From these results, we can extract two facts: first, that the starting point

significantly influences the convergence time, and second, that when the starting point is a bad point, OF2 offers a significant advantage. Certainly, it is not possible to know beforehand whether a starting point is a good or bad point; therefore, implementing a function such that it provides a faster convergence is the worst case and is the best optimization approach.

Finally, the parameters identified for the H-S model, when the OF1 and OF2 were used in the optimization are shown in Table 8 and Table 9 respectively. Additionally, to assess the quality of each solution, error measurements (AARE and RMSE) are provided on the bottom side of each table for every set of parameters. The best result was obtained when OF2 was used. It converged after 92 iterations, whereas the second-best result obtained with OF1 was achieved after 149 iterations. Although the quality of the best solutions obtained from each objective function is similar, there are some differences. For instance, parameter m_7 shows a difference, whereas parameter m_8 has comparable values. This behavior may indicate that the function has a flat zone, which causes the search algorithm to become stuck around that area. Another fact that supports the existence of this flat zone is that both answers have the same sign.

In contrast, the other results showed opposite signs for the same parameter compared to the best answer. It is worth mentioning that starting points 3 and 4 gave the worst answer quality for both objective functions. These values are entirely different regardless of the quality of the results; however, the search algorithm converged quickly in these cases, proving the minimum local existence. Thus, when the algorithm is stuck in a local minimum or finds the global one, the proposed objective function based on "true error" provides an advantage during the identification procedure. This advantage implies a shorter computing time and better parameter set after identification.

Table 8. Parameter determined for H-S equation using OF1 and their error.

Parameter	Starting point			
	1	2	3	4
m1	-5.25E-03	-4.41E-03	-3.16E-03	8.86E-03
m2	0.1618	0.1795	1.3581	0.5224
m4	4.23E-05	2.28E-05	5.78E-04	-1.51E-01
m5	3.30E-03	2.10E-03	-4.85E-03	-3.09E-01
m7	-2.717	-2.021	-0.241	1.679
m8	9.29E-05	9.40E-05	6.68E-05	1.17E-04
A	30851.34	15300.00	80698.27	50718.65
AARE-%	7.93	9.97	40.14	95.38
RMSE-[MPa]	9.60	12.64	47.63	117.52

Table 9. Parameter determined for H-S equation using OF2 and their error.

Parameter	Starting point			
	1	2	3	4
m1	-1.74E-03	-3.65E-03	-5.18E-03	-2.42E-02
m2	0.4868	0.2452	0.2535	0.2422
m4	7.20E-04	1.98E-04	1.89E-04	1.12E-04
m5	-4.95E-03	6.6E-04	1.76E-03	1.41E-03
m7	2.000	-1.194	-2.000	-1.625
m8	1.14E-04	1.02E-04	9.18E-05	-8.39E-03
A	2793.37	8659.98	42028.59	24037.65
AARE-%	14.30	7.58	15.41	77.28
RMSE-[MPa]	17.63	9.26	20.49	99.80

Finally, the parameters for the J-C model were identified using OF2, as mentioned previously. The results obtained are listed in Table 10 the results obtained for each starting point are shown. Error measurements are also included on the bottom side for each point. The J-C equation is straightforward compared to the H-S equation for identification because it requires only four parameters to be determined. As expected, the results were similar among them, and they exhibited identical quality. Thus, it can be concluded that the J-C equation has an absolute minimum in the specified search area, and the algorithm determines the minimum.

Table 10. Parameters identified for J-C equation.

Parameter	Starting point			
	1	2	3	4
B	100.00	124.57	124.33	124.36
n	0.1205	0.1286	0.1320	0.1320
C	0.1926	0.1507	0.1525	0.1525
q	1.1417	0.9634	0.9700	0.9710
AARE-%	13.91	13.16	13.17	13.17
RMSE [MPa]	18.74	17.19	17.35	17.35

4.6. Discussion of results

Although the AARE and RMSE factors provide a mathematical sense of the quality of the parameters, it is also essential to assess the results graphically. In Figure 23 up to Figure 25, the experimental and calculated results obtained for all experimental conditions are shown. The J-C model shows a good correlation at low strains; however as due to its mathematical formulation, it is not capable of catching the softening part, and continues showing a

hardening behavior. We can observe that the J-C model tends to underpredict the stress around the peak value and tends to overpredict on the steady state region.

On the other hand, it can be observed that the H-S equation predicts material behavior better than the J-C equations. Overall, it can catch the hardening until the peak stress value with good accuracy, then, the softening is also calculated; however, the model struggles to accurately represent the steady state region. This is because the H-S equation considers the factors for hardening and softening separately, whereas J-C does not. In addition, the H-S equation includes a term that considers the interaction between the temperature and strain rate.

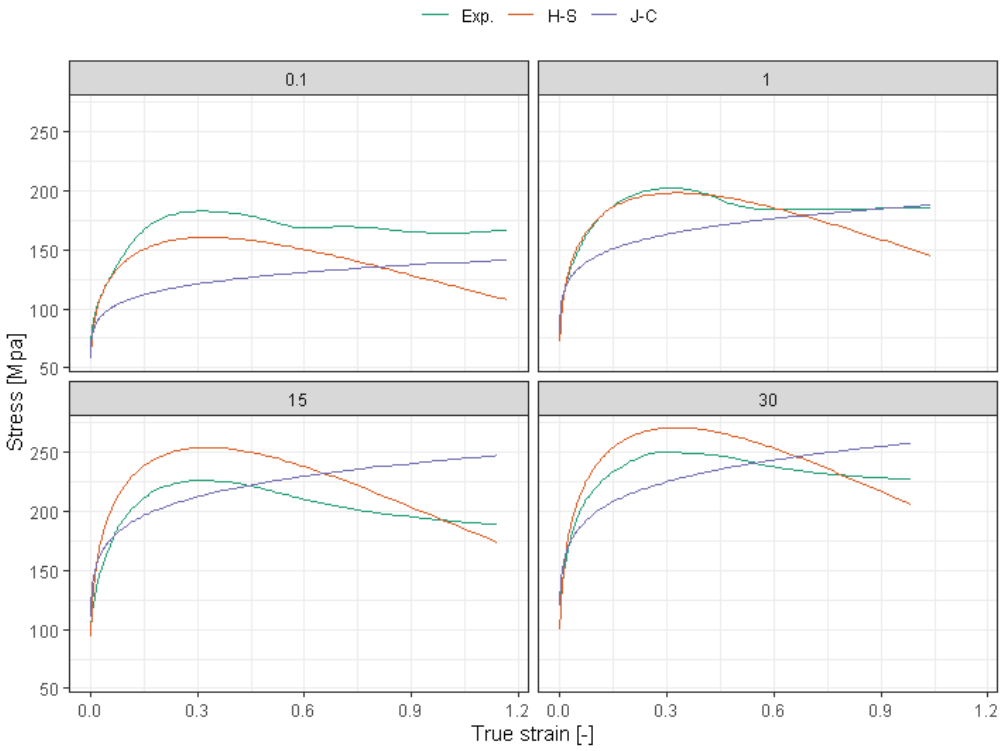

Figure 22. Experimental and calculated flow stresses for different strain rates at 900°C.

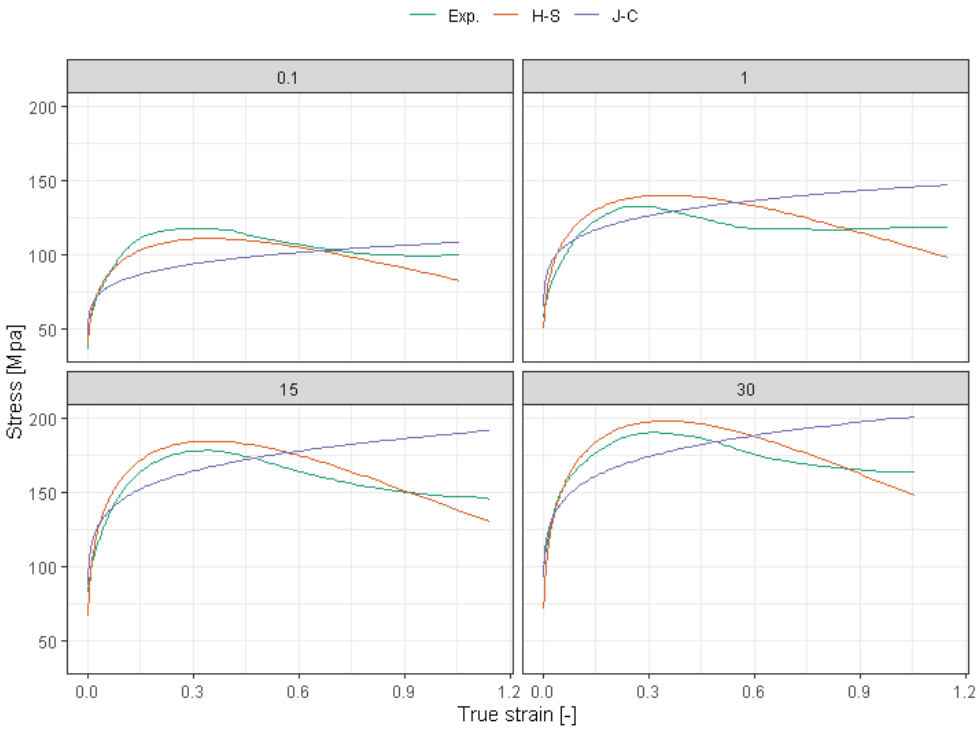

Figure 23. Experimental and calculated flow stresses for different strain rates at 1000°C.

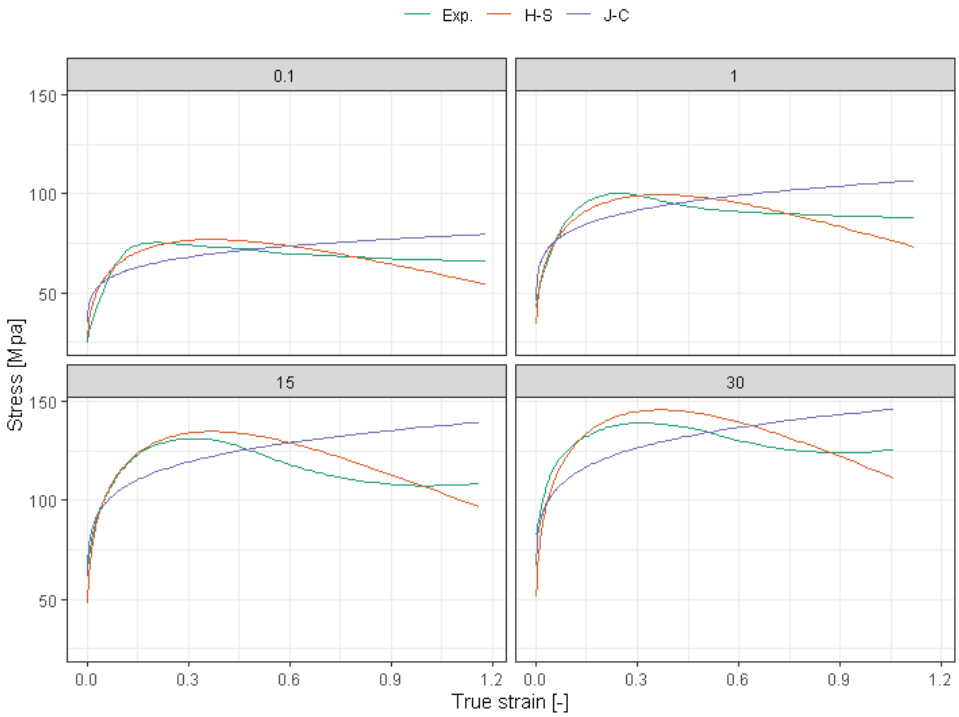

Figure 24. Experimental and calculated flow stresses for different strain rates at 1100°C.

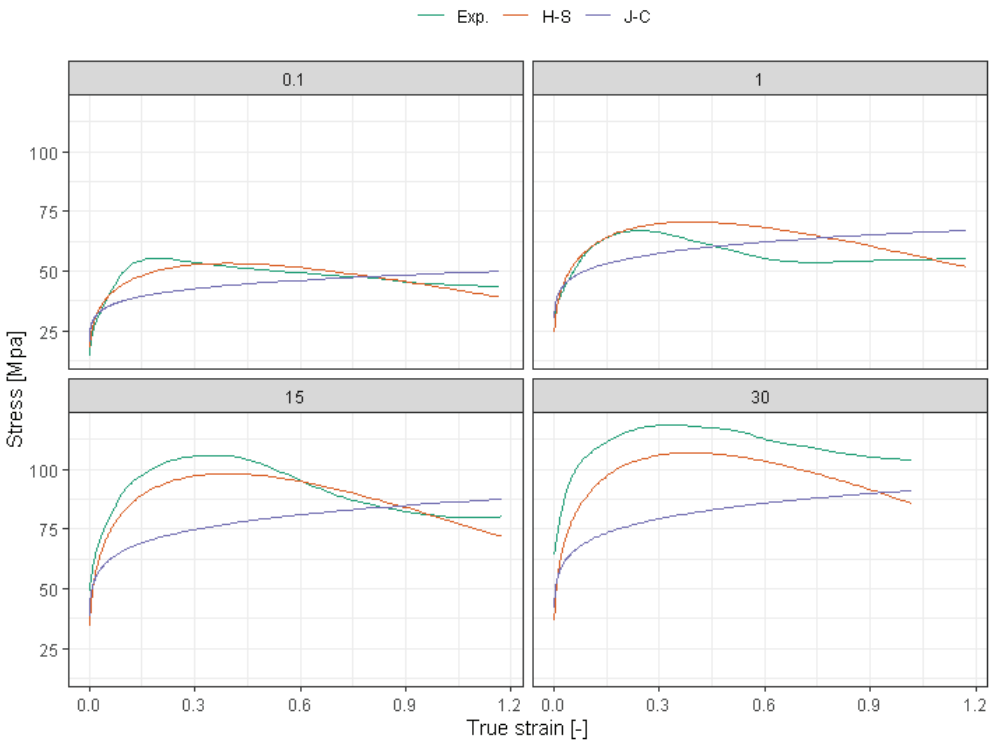

Figure 25. Experimental and calculated flow stresses for different strain rates at 1200°C.

As mentioned before, J-C does not possess the mathematical ability to predict softening properly, as it only considers these factors (temperature and strain rate) independently. It is worth noting that both constitutive equations struggle with softening predictions. The most common approach to overcome these difficulties is to consider the parameters as a function of strain by fitting polynomials. However, this approach has two drawbacks: the first increases the computational cost because the mathematical equation becomes more complex than the original equation; the second drawback is that polynomials are suitable for interpolation, but they perform poorly for extrapolations. Thus, modifying both equations to improve the softening behavior prediction is a good field for future research.

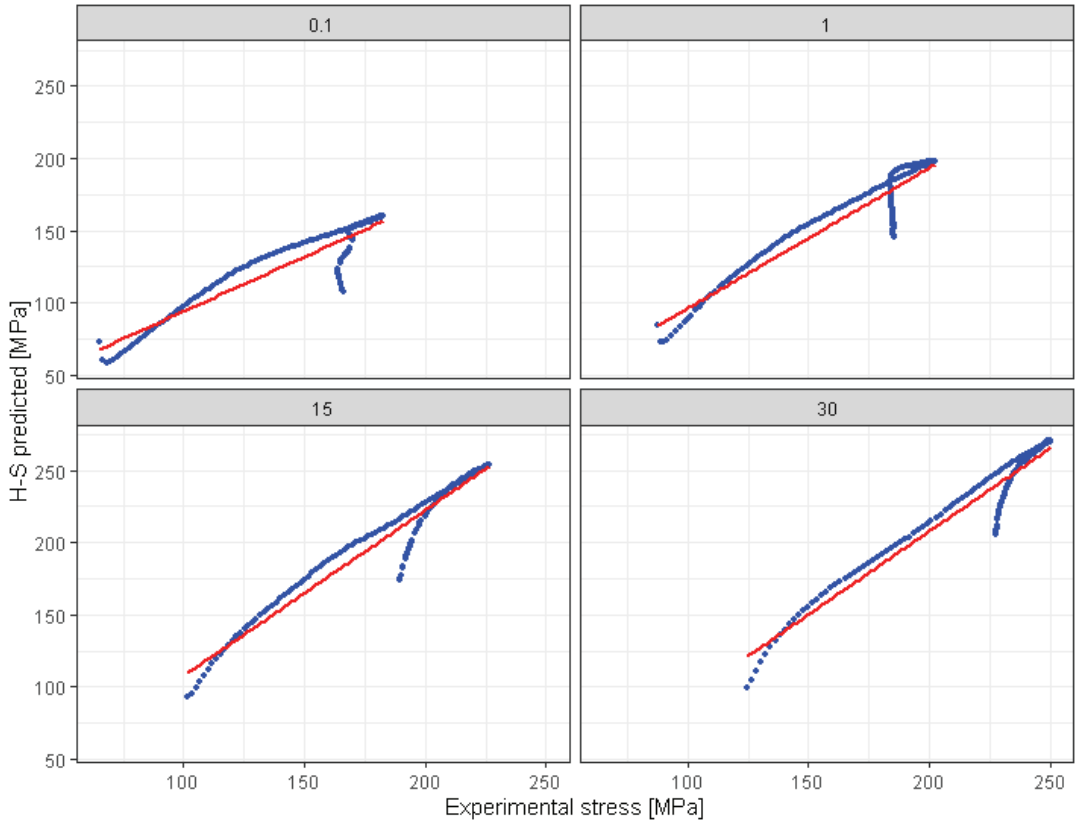

Figure 26. Calculated stress by H-S model vs the experimental value at 900°C.

The regression coefficient for all experimental condition is shown in Table 11. The H-S model shows a similar behavior over the entire range of experimental conditions, particularly at high strain rates. On the other hand, the J-C model shows a better performance at lower temperatures; this is since hardening is more pronounced at lower temperatures, with minimum softening region. Overall, for all experimental conditions, the H-S model has better correlation when compared with J-C model.

Table 11. Regression coefficient for H-S and J-C model's output.

Temperature [°C]	Strin rate [1/s]	R^2	
		H-S	J-C
900	0.1	0.856	0.821
	1	0.891	0.805
	15	0.944	0.688
	30	0.942	0.775
1000	0.1	0.970	0.735
	1	0.884	0.698
	15	0.963	0.615
	30	0.980	0.681
1100	0.1	0.908	0.692
	1	0.934	0.715
	15	0.958	0.544
	30	0.976	0.686
1200	0.1	0.941	0.659
	1	0.865	0.512
	15	0.945	0.572
	30	0.968	0.701

5. CONCLUSIONS AND OUTLOOK

The following conclusions were drawn from this study:

A successful and fast procedure for material parameter identification in industrial applications is described and it depicted in Appendix A. This procedure saves computational effort and time, providing reliable answers in a short time (in the order of minutes). In contrast, the traditional approach for connecting the finite element model with optimization algorithms involves nonlinear models. The latter approach is highly time-consuming because several models must be solved, which increases exponentially with the number of parameters.

A new objective function based on the true error was proposed for faster material parameter identification. This new function was compared with another based on the classical least square approach. It was found that the proposed function has a faster performance, which means that it converges rapidly to the solution. Several starting points were tried to assess the objective function performance.

The parameters for two commonly used constitutive equations in industrial applications were identified: the Hensel-Spittel (H-S) equation and Johnson-Cook (J-C) equation. The latter uses four parameters, and the former uses eight parameters. The H-S equation had several local minima. In contrast, the J-C equations showed a convergence towards the same minimum, which means that an absolute minimum exists. This is understandable because H-S is much more complex, as long as it has twice the number of parameters than J-C.

With the basis on the quality assessment done by using the AARE and the RMSE, the best set of parameters for the H-S equation was obtained when OF2 and starting point 2 were used (see Table 9). In contrast, the J-C equation showed the best quality at starting point 2 (Table 10). In the latter case, only this objective function was used because OF2 was previously determined to have better performance. In addition, we can observe the H-S model has a stable correlation across all experimental conditions, whereas the J-C model decreases its performance when the temperature increases. This is due to the fact that softening becomes more prominent with temperature, and the J-C model does not possess the mathematical ability to catch this properly.

As a result of the analysis detailed in the first paper listed in Appendix B, and summarized in Appendix D, it was possible to demonstrate that the results obtained by using the Arbitrary Lagrangian and Eulerian (ALE) approach are as accurate as the ones obtained when the classical Lagrangian is utilized. This opens the door to analysis that can consider the generation of oxide scales in the material when forged at high temperature, as it was shortly described in the last part of the Appendix D, where a simple ALE multi material model is presented, showing the steel matrix and the three different oxides layers.

In further steps, we may mention that it is necessary to determine a modification for the constitutive equation. The aim of this modification is to provide them with the ability to catch the softening produced by dynamic recrystallization (DRX). This ability is convenient for metal forming simulations. Additionally, it is necessary to conduct more experiments using the same material to assess the performance of the identified parameters for interpolations and extrapolations. Moreover, the H-S equation needs to be integrated into the LS-Dyna by developing a user subroutine.

Additionally, since the approach was confirmed to deliver accurate results as well as capable to simulate multi material problems, another field of study is to develop methods that allow to simulate problems with oxide scales. This will allow for a better frictional characterization when reverse engineering is applied.

REFERENCES

[1] L. Heng and F. Mingwang, "Chapter 1 - Introduction to Deformation-Based Manufacturing," in *Deformation-Based Processing of Materials*, Elsevier, 2019, pp. 1-28.

[2] ASM Internation, Cold and Hot Forging Fundamental and Applications, T. Altan, G. Ngaile and G. Shen, Eds., Materials Park, OH, 2005.

[3] EUROFORGE, "EUROFORGE WEBSITE," EUROFORGE AISBL, [Online]. Available: https://www.euroforge.org/activities-and-projects/. [Accessed 27 7 2023].

[4] U. S. Dixit, "1 - Modeling of metal forming: a review," in *Mechanics of Materials in Modern Manufacturing Methods and Processing Techniques*, V. V. Silberschmidt, Ed., Elsevier, 2020, pp. 1-30.

[5] G. Z., P. Z., M. L., G. A., L. L., Ł.-S. A., Ł. J., M. S., M. Z., M. W., P. M., Ś. R.E., T. J., W. S., W. G., Z. J. and Z. S., "Recent development trends in metal forming," *Archives of Civil and Mechanical Engineering,* vol. 19, no. 3, pp. 898-941, 2019.

[6] A. Andrade-Campos, S. Coppieters and M. Strano, "Optimization and inverse analysis in metal forming: scientific state-of-the-art and recent trends," *International Journal of Material Forming,* vol. 15, no. 44, 2022.

[7] C. L. Y., C. Ming-Song and Z. Jue, "Prediction of 42CrMo steel flow stress at high temperature and strain rate," *Mechanics Research Communications,* vol. 35, no. 3, pp. 142-150, 2008.

[8] Q. Guo-Zheng, "Characterization for Dynamic Recrystallization Kinetics Based on Stress-Strain Curves," in *Recent Developments in the Study of Recrystallization*, P. Wilson, Ed., IntechOpen, 2013, pp. 61-88.

[9] M. Krbaťa, M. Eckert, D. Križan, I. Barényi and I. Mikušová, "Hot Deformation Process Analysis and Modelling of X153CrMoV12 Steel," *Metals,* vol. 9, no. 10, p. 1125, 2019.

[10] X. Zhou, W. Ma, C. Feng and L. Zhang, "Flow stress modeling, processing maps and microstructure evolution of 05Cr17Ni4Cu4Nb Martensitic stainless steel during hot plastic deformation," *Mater. Res. Express,* vol. 7, no. 4, pp. 1-14, 2020.

[11] B. Chaparro, S. Thuillier, L. Menezes, P. Manach and J. Fernandes, "Material parameters identification: Gradient-based, genetic and hybrid optimization algorithms," *Computational Materials Science,* vol. 44, no. 2, pp. 339-346, 2008.

[12] R. Christian, R. Thomas, K. Günter, K. Andre and W. Frank, "Development of a standard calibration procedure for the DEM parameters of cohesionless bulk materials – Part II: Efficient optimization-based calibration," *Powder Technology,* vol. 360, pp. 967-976, 2020.

[13] D. H. Wolpert and W. G. Macready, "No free lunch theorems for optimization," *IEEE Transactions on Evolutionary Computation,* vol. 1, no. 1, pp. 67-82, 1997.

[14] J. A. Nelder and E. Mead, "A Simplex Method for Function Minimization," *The Computer Journal,* vol. 7, no. 4, pp. 308-313, 1965.

[15] N. Amoura, H. Kebir and A. Benzerdjeb, "3D crack identification using the Nelder-Mead Simplex algorithm combined with a random generation of crack positions," *Frattura ed Integrità Strutturale,* vol. 16, no. 55, pp. 243-255, 2021.

[16] M. Hardt, D. Schraknepper and T. Bergs, "Investigations on the Application of the Downhill-Simplex-Algorithm to the Inverse Determination of Material Model Parameters for FE-Machining Simulations," *Simulation Modelling Practice and Theory,* vol. 107, 2021.

[17] R. de-Carvalho, R. Valente and A. Andrade-Campos, "Optimization strategies for non-linear material parameters identification in metal forming problems," *Computers & Structures,* vol. 89, no. 1-2, pp. 246-255, 2011.

[18] T. FURUKAWA and G. YAGAWA, "INELASTIC CONSTITUTIVE PARAMETER IDENTIFICATION USING AN EVOLUTIONARY ALGORITHM WITH CONTINUOUS INDIVIDUALS," *Int. J. Numer. Meth. Engng.,* vol. 40, no. 6, pp. 1071-1090, 1997.

[19] A. R. Yildiz, "Comparison of evolutionary-based optimization algorithms for structural design optimization," *Engineering Applications of Artificial Intelligence,* vol. 26, no. 1, pp. 327-333, 2013.

[20] T. Bäck and H.-P. Schwefel, "An Overview of Evolutionary Algorithms for Parameter Optimization," *Evolutionary Computation,* vol. 1, no. 1, pp. 1-23, 1993.

[21] J. Cao and J. Lin, "A study on formulation of objective functions for determining material models," *International Journal of Mechanical Sciences,* vol. 50, no. 2, pp. 193-204, 2008.

[22] A. C. Andrade, R. de-Carvalho and R. A. Valente, "Novel criteria for determination of material model parameters," *International Journal of Mechanical Sciences,* vol. 54, no. 1, pp. 294-305, 2012.

[23] K. Ghobadi and H. Mahmoudzadeh,, "Inferring linear feasible regions using inverse optimization," *European Journal of Operational Research,* vol. 290, no. 3, pp. 829-

843, 2021.

[24] J.-C. a. G. O. Gelin, "An inverse solution procedure for material parameters identification in large plastic deformations," *Commun. Numer. Meth. Engng.,* vol. 12, no. 3, pp. 161-173, 1996.

[25] N. Souto, A. Andrade-Campos and S. Thuillier, "Material parameter identification within an integrated methodology considering anisotropy, hardening and rupture," *Journal of Materials Processing Technology,* vol. 220, pp. 157-170, 2015.

[26] M. Rolf and S. Erwin, "Parameter identification for viscoplastic models based on analytical derivatives of a least-squares functional and stability investigations," *International Journal of Plasticity,* vol. 12, no. 4, pp. 451-479, 1996.

[27] N. Z. Sun and A. Y. Sun, "Inverse Methods for Parameter Estimations," *Encyclopedia of hydrological sciences,* 2006.

[28] A. Shrot and M. Bäker, "A Study of Non-uniqueness During the Inverse Identification of Material Parameters," *Procedia CIRP,* vol. 1, pp. 72-77, 2012.

[29] A. Seupel, G. Hütter and M. Kuna, "On the identification and uniqueness of constitutive parameters for a non-local GTN-model," *Engineering Fracture Mechanics,* vol. 229, 2020.

[30] Y. Zhang, A. Van-Bael, A. Andrade-Campos and S. Coppierters, "Parameter identifiability analysis: Mitigating the non-uniqueness issue in the inverse identification of an anisotropic yield function," *International Journal of Solids and Structures,* vol. 243, 2022.

[31] M. Rolf and E. Stein, "A unified approach for parameter identification of inelastic material models in the frame of the finite element method," *Computer Methods in Applied Mechanics and Engineering,* vol. 136, no. 3-4, pp. 225-258, 1996.

[32] T. Harth and J. Lehn, "Identification of Material Parameters for Inelastic Constitutive Models Using Stochastic Methods," *GAMM-Mitteilungen,* vol. 30, no. 2, pp. 403-429, 2017.

[33] S.-d. Gu, L.-w. Zhang, J.-h. Ruan, P.-z. Zhou and Y. Zhen, "Constitutive Modeling of Dynamic Recrystallization Behavior and Processing Map of 38MnVS6 Non-Quenched Steel," *J. of Materi Eng and Perform,* vol. 23, p. 1062–1068, 2014.

[34] S. Gu, L. Zhang, C. Zhang, J. Ruan and Y. Zhen, "Modeling the Effects of Processing Parameters on Dynamic Recrystallization Behavior of Deformed 38MnVS6 Steel," *Journal of Materials Engineering and Performance,* vol. 24, no. 5, p. 1790–1798 , 2015.

[35] R. S. NALAWADE, V. R. MARJE, G. BALACHANDRAN and V. BALASUBRAMANIAN, "Effect of pass schedule and groove design on the metal deformation of 38MnVS6 in the initial passes of hot rolling," *Sadhana,* vol. 41, no. 1, pp. 111-124, 2016.

[36] N. Dexue, Z. Jian, X. Peiyou, H. Guannan, L. Shiying and W. Guo, "High temperature fatigue and oxidation characteristics of forged steel piston materials," *Engineering Failure Analysis,* vol. 97, pp. 220-226, 2019.

[37] E. Y. and S. N., "The effect of thermomechanical process on metallurgical and mechanical properties of 38MnVS6 micro alloyed steel," *Material Science & Engineering Techonology,* vol. 52, pp. 644-654, 2021.

[38] TA Instruments, [Online]. Available: https://www.tainstruments.com/. [Accessed 4 12 2023].

[39] G. Korpala, *Comparison of different measuring systems of flow curves,* Freiberg, Germany, 2016.

[40] M. H., M. C. J., M. P. J. and N. A., "Hot deformation behavior of a medium carbon microalloyed steel," *Materials Science and Engineering: A,* vol. 528, no. 10-11, pp. 3876-3882, 2011.

[41] W. Guobing, P. Xiaodong, H. Amir, M. Yahya, X. Weidong, Y. Yan and A. W. Mary, "Constitutive modeling of Mg–9Li–3Al–2Sr–2Y at elevated temperatures," *Mechanics of Materials,* vol. 89, pp. 241-253, 2015.

[42] J. S. M., R. S. T., W. L. A., E. B. D., C. A. R. and A. B. R., "A new mixed finite element method for viscoelastic flows governed by differential constitutive equations," *Journal of Non-Newtonian Fluid Mechanics,* vol. 59, no. 2-3, pp. 215-243, 1995.

[43] C. L. Y. and C. Xiao-Min, "A critical review of experimental results and constitutive descriptions for metals and alloys in hot working," *Materials & Design,* vol. 32, no. 4, pp. 1733-1759, 2011.

[44] Z. Hui and O. Hengan, "Constitutive modelling of hot deformation behaviour of metallic materials," *Materials Science and Engineering: A,* vol. 832, 2022.

[45] J. Trajkovski, R. Kunc, V. Pepel and I. Prebil, "Flow and fracture behavior of high-strength armor steel PROTAC 500," *Materials & Design,* vol. 66, pp. 37-45, 2015.

[46] M. Zamani, H. Dini, A. Svoboda, L.-E. Lindgren, S. Seifeddine, N.-E. Andersson and A. E. Jarfors, "A dislocation density based constitutive model for as-cast Al-Si alloys: Effect of temperature and microstructure," *International Journal of Mechanical Sciences,* vol. 121, pp. 164-170, 2017.

[47] Y. Kangbo, Y. Xiaohu, Y. Yongqi, W. Ruifeng, C. Zishu, Z. Kexuan and W. Zhijun, "Dynamic thermomechanical response and constitutive modeling of eutectic high-entropy alloy," *International Journal of Mechanical Sciences,* vol. 246, 2023.

[48] A. H., L. R., W. M., K. R., G. M., M. V., P. G. and G. G., "Integration of physically based models into FEM and application in simulation of metal forming processes," *Modelling Simul. Mater. Sci. Eng. ,* vol. 8, no. 6, 2000.

[49] A. Svoboda, D. Wedberg and L.-E. Lindgren, "Simulation of metal cutting using a physically based plasticity model," *Modelling Simul. Mater. Sci. Eng.,* vol. 18, no. 7, 2010.

[50] S. K. Akhtar and H. Sujian, "Experimental and theoretical study of mechanical behavior of 1100 aluminum in the strain rate range 10−5−104s−1," *International Journal of Plasticity,* vol. 8, no. 4, pp. 397-424, 1992.

[51] G. R. Johnson and W. H. Cook, "Fracture characteristics of three metals subjected to various strains, strain rates, temperatures and pressures," *Engineering Fracture Mechanics,* vol. 21, no. 1, pp. 31-48, 1985.

[52] N. Nam and H. Ali, "Direct calculation of Johnson-Cook constitutive material parameters for oblique cutting operations," *Journal of Manufacturing Processes,* vol. 92, pp. 226-237, 2023.

[53] J. Zhe, G. Ben, Z. Yong, W. Yuan and M. Lei, "Modified Johnson-Cook model of aluminum alloy 6016-T6 sheets at low dynamic strain rates," *Materials Science and Engineering: A,* vol. 820, 2021.

[54] P. Joshua, G. Hassan, A.-S. Sabino, L. Anders and W. Matthew, "A modified Johnson-Cook constitutive model for improved thermal softening prediction of machining simulations in C45 steel," *Procedia CIRP,* vol. 108, pp. 106-111, 2022.

[55] A. Hensel and T. Spittel, Kraft- und Arbeitsbedarf bildsamer Formgebungsverfahren, Leipzig: VEB DeutscherVerlag fur Grundstoffindustrie, 1978.

[56] P. Tize Mha, P. Dhondapure, M. Jahazi, A. Tongne and O. Pantalé, "Interpolation and Extrapolation Performance Measurement of Analytical and ANN-Based Flow Laws for Hot Deformation Behavior of Medium Carbon Steel," *Metals,* vol. 13, no. 3, 2023.

[57] R. André, S. Peter, J. Martin and G. Carsten, "Constitutive modelling of the 6061 aluminium alloy under hot rolling conditions and large strain ranges," *Materials & Design,* vol. 190, 2020.

[58] S. A., Z.-H. A., G. M. and M. S., "The high temperature flow behavior modeling of NiTi shape memory alloy employing phenomenological and physical based

constitutive models: A comparative study," *Intermetallics,* vol. 53, pp. 140-149, 2014.

[59] Altair, "HyperStudy Home Page," [Online]. Available: https://www.altair.com.es/hyperstudy/. [Accessed 22 Oct. 2023].

[60] QForm Group, [Online]. Available: https://www.qform3d.com/. [Accessed 03 2021].

[61] ANSYS, "ANSYS LS-Dyna," [Online]. Available: https://www.ansys.com/products/structures/ansys-ls-dyna?utm_source=google&utm_medium=ppc&utm_campaign=brand&utm_content=digital_structures_learn-more_ansys-lsdyna_ad-a&utm_term=ansys%20ls-dyna&campaignid=7013g000000kn6oAAA&creative=474223716670&keyword=an. [Accessed 4 2021].

[62] K. Sedighiani, M. Diehl, K. Traka, F. Roters, J. Sietsma and D. Raabe, "An efficient and robust approach to determine material parameters of crystal plasticity constitutive laws from macro-scale stress–strain curves," *International Journal of Plasticity,* vol. 134, 2020.

[63] QuantorForm Ltd, "QForm Software," [Online]. Available: https://www.qform3d.com/. [Accessed 8 12 2023].

APPENDIX

Appendix A. Flowchart for the optimization framework.

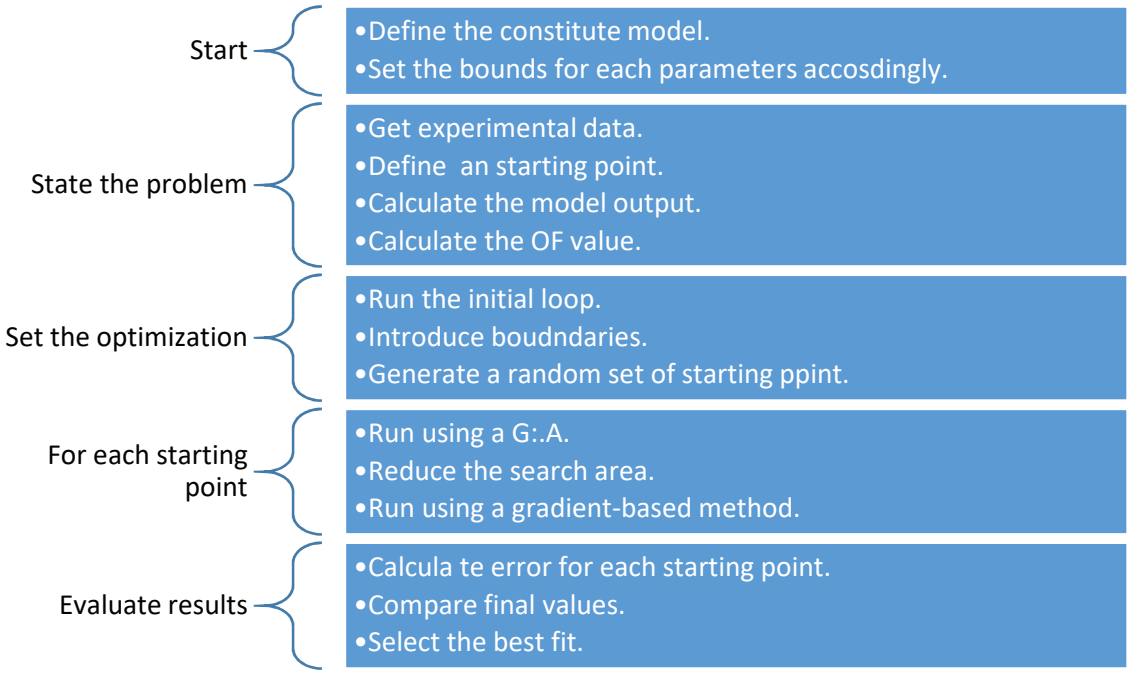

Appendix B. List of publications.

The following is a list of papers published as a result of the present research:

- Gomez-Marquez, D., Ledesma-Orozco, E., Hino, R. et al. Numerical study on the hot compression test for bulk metal forming application. SN Appl. Sci. 4, 220 (2022). https://doi.org/10.1007/s42452-022-05093-x.
- Gomez-Marquez, D., Ledesma-Orozco, E., Hino, R., Aguilera-Gomez, E., Hamasaki, H.. (2022). IDENTIFICATION OF PARAMETERS FOR CHARACTERIZATION AT HIGH-TEMPERATURE OF 38MnVS6 STEEL USED IN HOT FORGING PROCESSES. DYNA, 97(3). 288-294. DOI: https://doi.org/10.6036/10371.
- Gomez, D, Ledesma, E, Hino, R, Hamasaki, H, Aguilera, E, & Ruiz, I. "Friction Assessment in Hot Forging Operations Using Large-Scale Ring Compression Test." Proceedings of the ASME 2021 International Mechanical Engineering Congress and Exposition. Volume 2A: Advanced Manufacturing. Virtual, Online. November 1–5, 2021. V02AT02A054. ASME. https://doi.org/10.1115/IMECE2021-71851.

Appendix C: Experimental temperature during hot compression test.

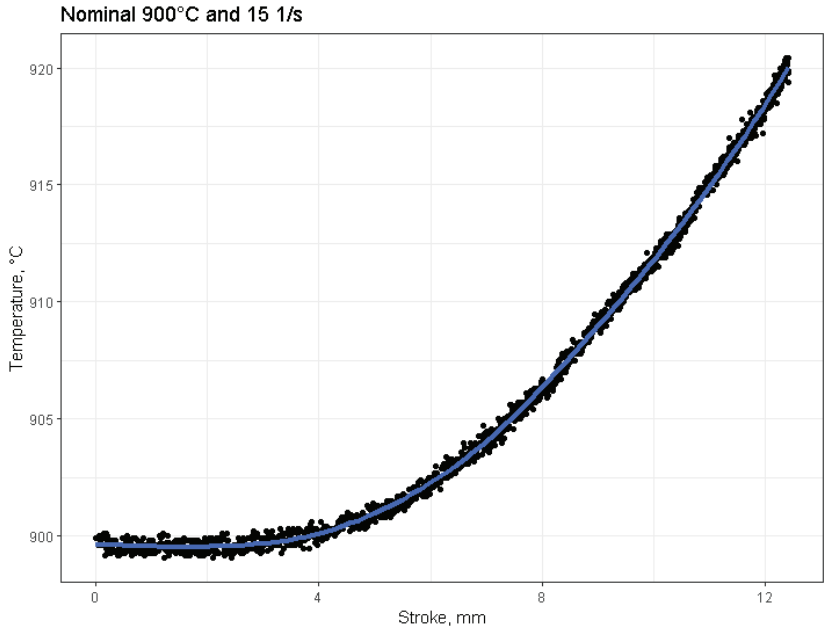

Figure C1: temperature for 900 °C and 15 s^{-1}.

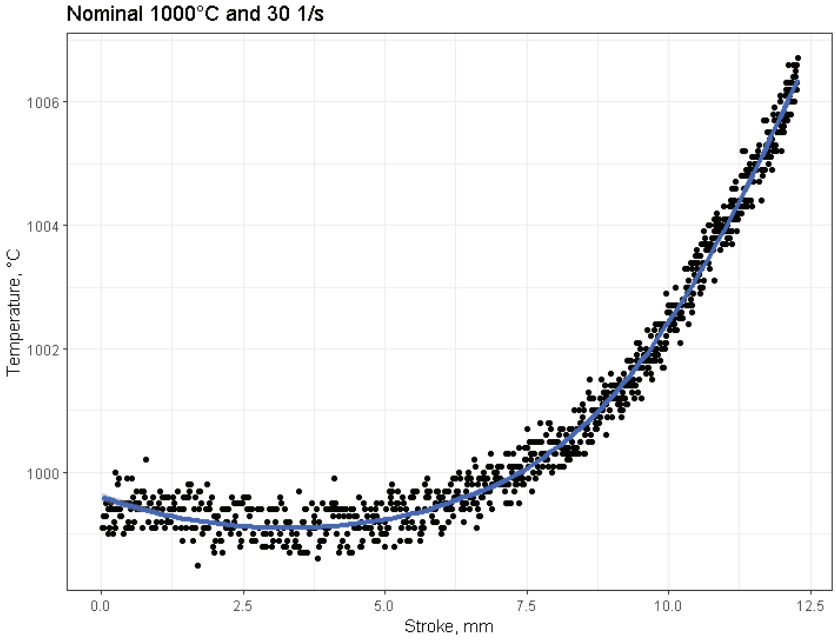

Figure C2: temperature for 1000°C and 30 s^{-1}.

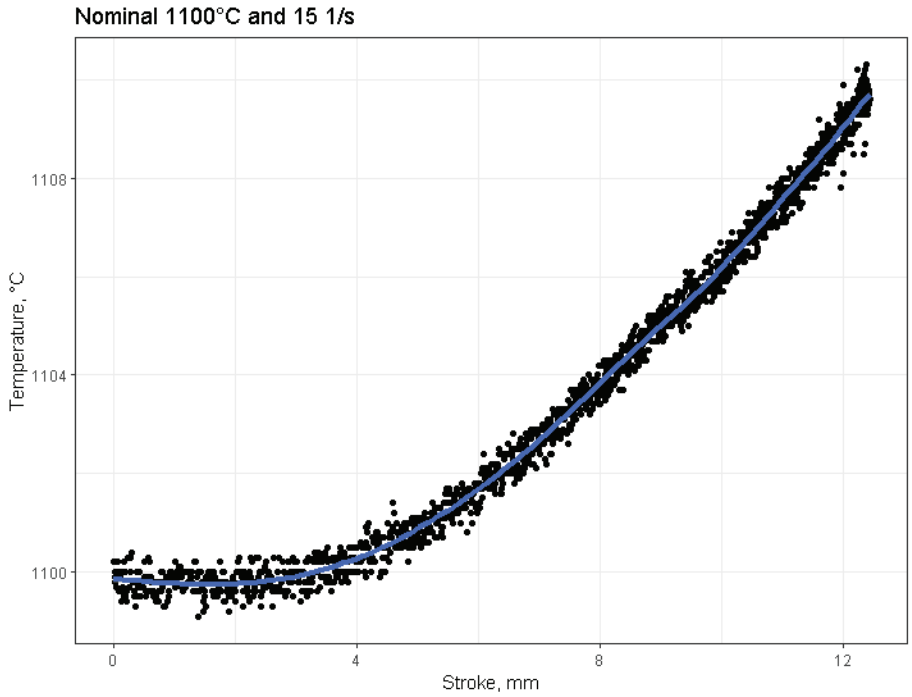

Figure C3: temperature for 1100°C and 15 s^{-1}.

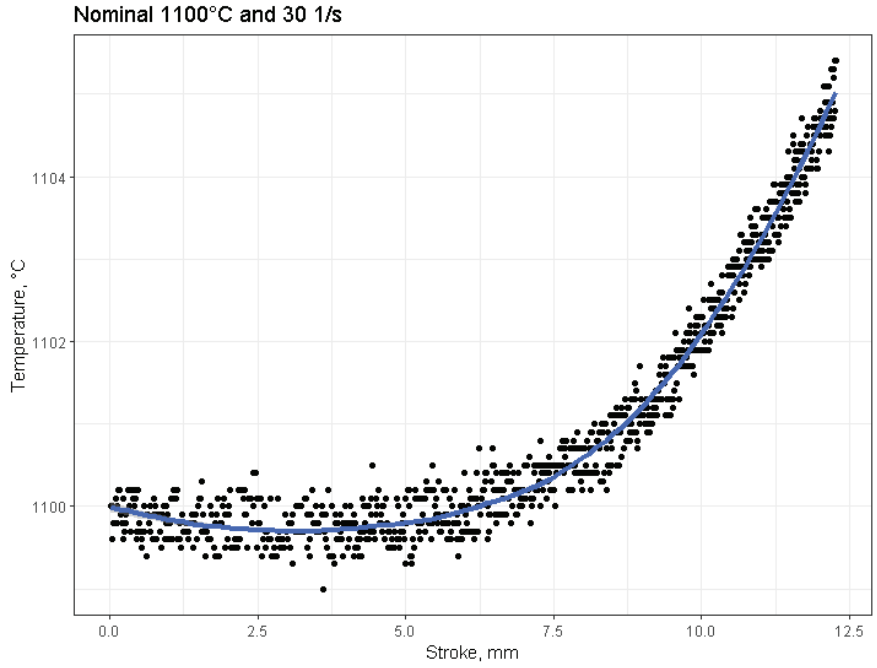

Figure C4: temperature for 1100°C and 30 s^{-1}.

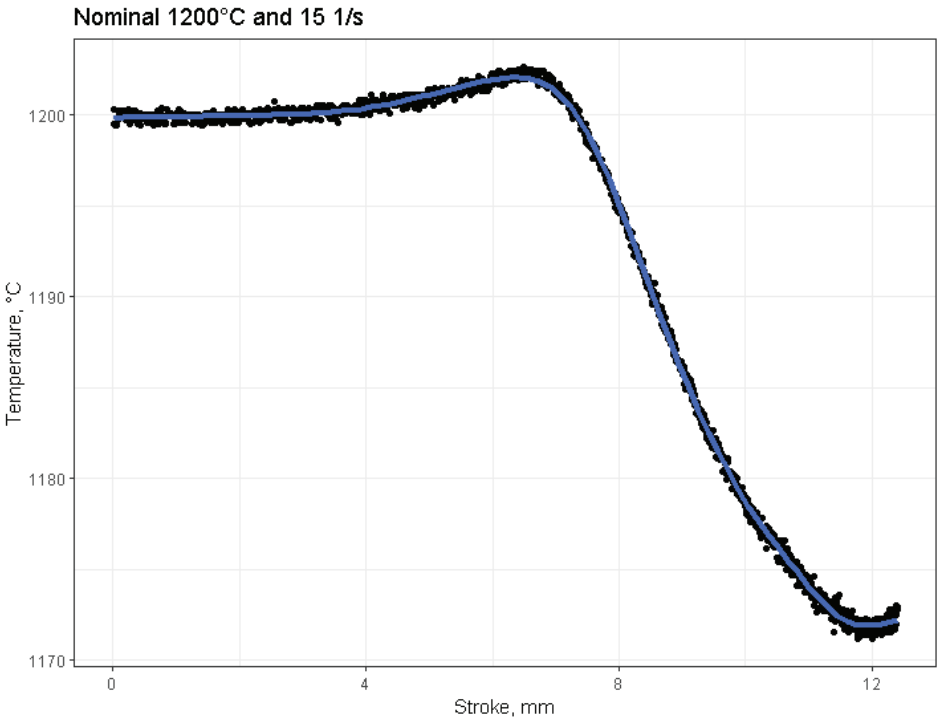

Figure C5: temperature for 1200°C and 15 s^{-1}.

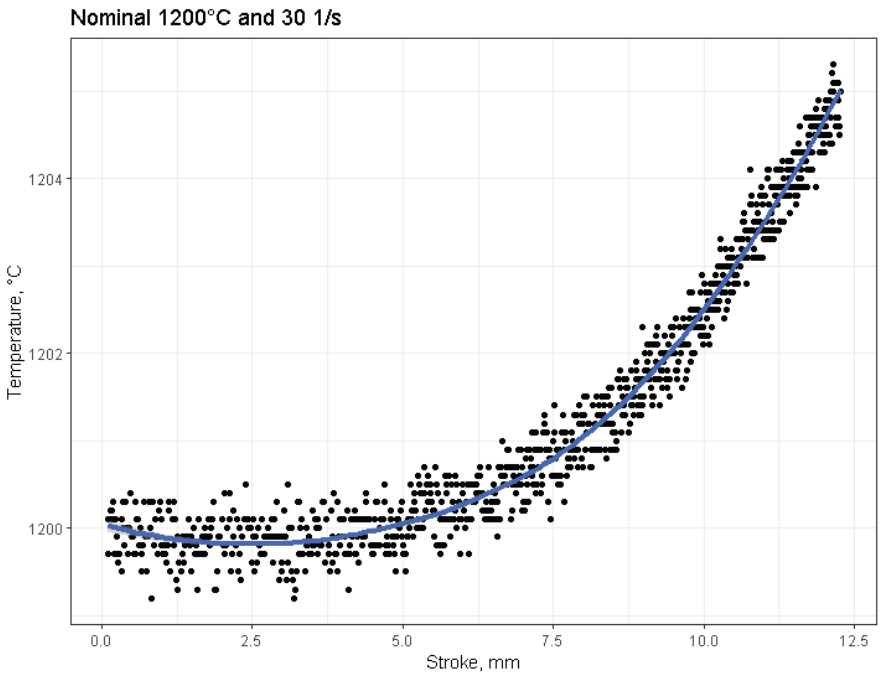

Figure C6: temperature for 1200°C and 30 s^{-1}.

Appendix D: Case of study on the Finite Element Model

As an application example, the identified parameters were used in a Finite Element Model (FEM). For this study, two software packages were used for finite element modeling: QForm (QuantorForm Ltd) [60] and LS-DYNA (Ansys) [61]. The former is a widely used software in the metal forming industry designed for its specific purposes and already integrates the H-S model. The latter is widely used software for general non-linear purposes. In order to address the large deformation and the nonlinearities involved in the present study, two approaches were used and compared, i.e., every software has its approach: QForm uses the classical re-meshing technique, whereas in LS-Dyna the Arbitrary Lagrangian-Eulerian approach was selected. In addition, for the sake of brief, numerical simulations were carried out only for the strain rates of 15 and 30 s^{-1}, which correspond to 68 and 34 milliseconds in experiment duration, respectively. Even though two different software packages were used, some aspects are similar for both, e.g., the problem is non-linear, and thermos-mechanical coupled. A three-dimensional model using solid elements is used. A quarter of symmetry was specified.

An overview of spatial discretization is given in Figure D1 a) for the QForm model and Figure D1 b) for the LS-Dyna model. The QForm model uses 3D elements for the anvils, whereas the LS-Dyna model used shell elements with thickness. In both cases the lower tool is fixed and the upper one is assigned with the velocity profile described in Section 3.3. in addition, the LS-Dyna requires a void volume which is capable to receive mass from the original volume.

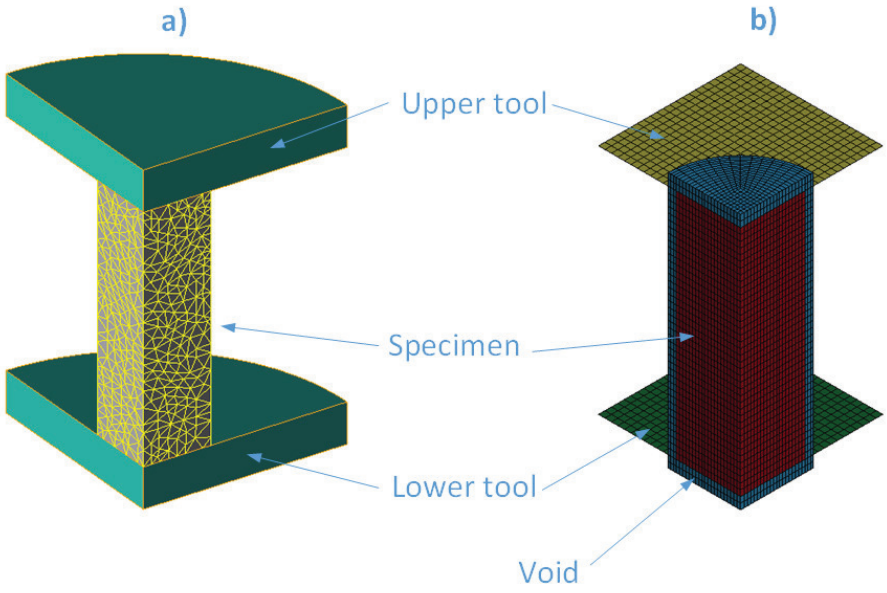

Figure D1: Finite element models: (a) QForm and (b) LS-Dyna.

The flow curves obtained from the experiments Section 3.4 are appropriately introduced in the database for the LS-Dyna model. The plastic flow is given as a function of strain, strain rate, and temperature. Whereas for the QForm model, in total, 8471 nodes with 40574 tetrahedron elements were used. The remeshing takes into account the deformation and temperature changes as criteria for rebuilding the mesh. The maximum optimal element's size was determined as 1 mm. In contrast, the software algorithm chose the minimum size automatically (although it is possible to set it).

Validation is then realized by comparing the calculated force vs. stroke curves measured during the experiments and those calculated by the finite element models. This comparison of the results shows a good agreement between the numerical with the experiments. Figure D2 shows four selected cases for discussion. From cases *a)* and *b)* is clear that at the same temperature, the strain rate slightly increases the force. Some discrepancies are evident at the beginning of compression. A possible explanation is an inertial effect imposed at first during the compression, as can be observed in cases *c)* and *d)*; with the temperature rise, the material workability increases, which means less force is required. Considering only the strain rate is also clear that lower values, which imply lower velocities, lead to less demanded power, and consequently, better equipment performance during compression. On the other hand, numerical results do not exhibit this behavior. Numerical models are set up with the ideal velocity profile to achieve a constant strain rate. This set up leads to variation during a short time in the kinetic energy (but it does not affect applied force) during the beginning of simulation. These differences may explain why there are some discrepancies during the first part of the load stroke curves.

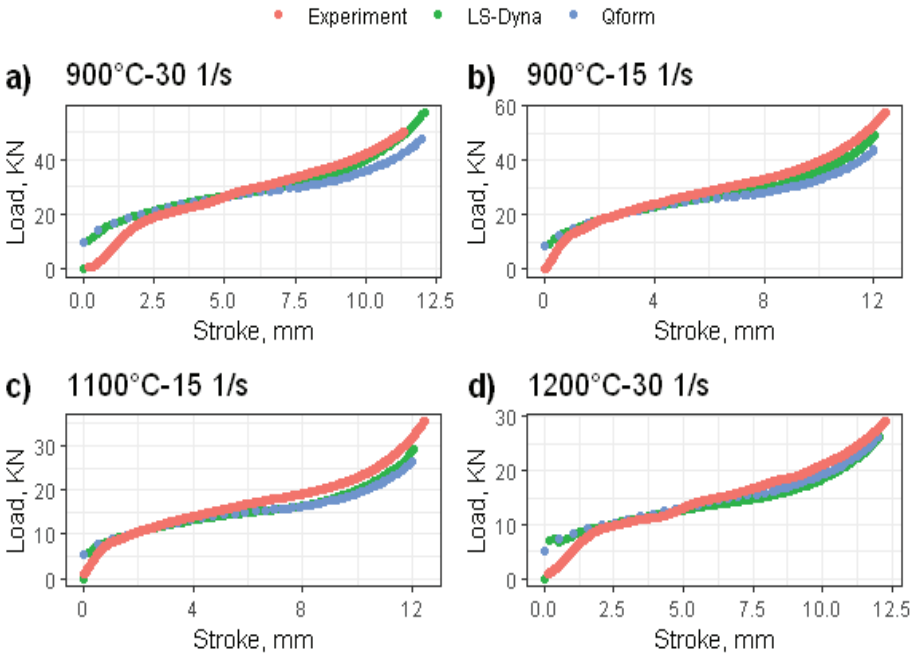

Figure D2: Load vs. stroke results for selected cases.

For comparison purposes, Figure D3 shows strain and stress contours, calculated at the final compression stage by both QForm and LS-Dyna for the condition of 900 °C and 30 1/s. All cases exhibit the same response, characterized by the so-called dead metal zone (the neighborhood to the contact zone), the shear bands (because of the metal folding over), and finally, the hydrostatic area (at the center, with the highest strain concertation). In Figure D3 a) and b), it is clear the strain output is similar from both software. However, there are slight differences in the stress, as shown in Figure D3 c) and d). These differences might be because the constitutive equation is not the same, as well as some differences in the element type. However, the maximum and minimum stress values calculated by both approaches are similar. Hence, it may be considered that both provided equivalent answers.

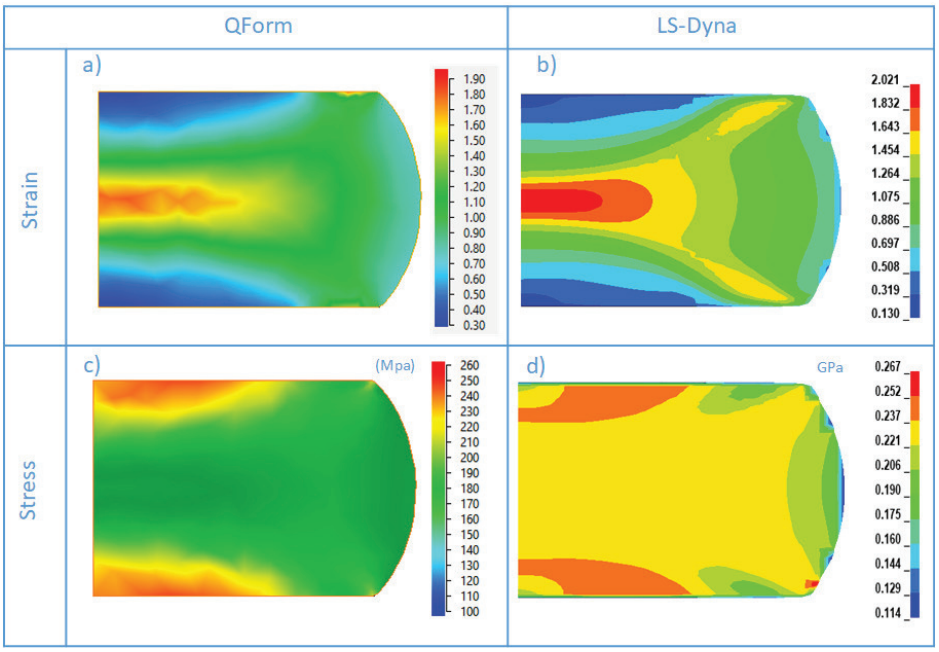

Figure D3: Calculated strain and stress (effective) at the end of the compression.

Based on the above results, it can be proved that the ALE approach achieves the same results as the classical Lagrangian approach. However, the classical Lagrangian approach is not capable to model multi material analysis, i.e. processes where more than one material exist inside a single element (like oxide scale formation), or where the material is from one element to another (like dissimilar material welding). It is well known that when still is heated, oxide scale appears with three different oxides: wustite, magnetite and hematite.

The oxide scale model in a simplified manner is shown in Figure D4 (left side), where the main part is a steel matrix (green body), and three different layers are added to consider the different oxides described before: yellow, brown, and red for wustite, magnetite and hematite, respectively. The purpose of this simplified model is to prove the capabilities

(without validation) of the ALE approach to model this problem. In this case, the stress (GPa) is shown on the right-side picture, and it is simple to observe the discontinuity on the stress field at the interfaces of the different oxide's layers. The reason for this is because each layer behaves differently.

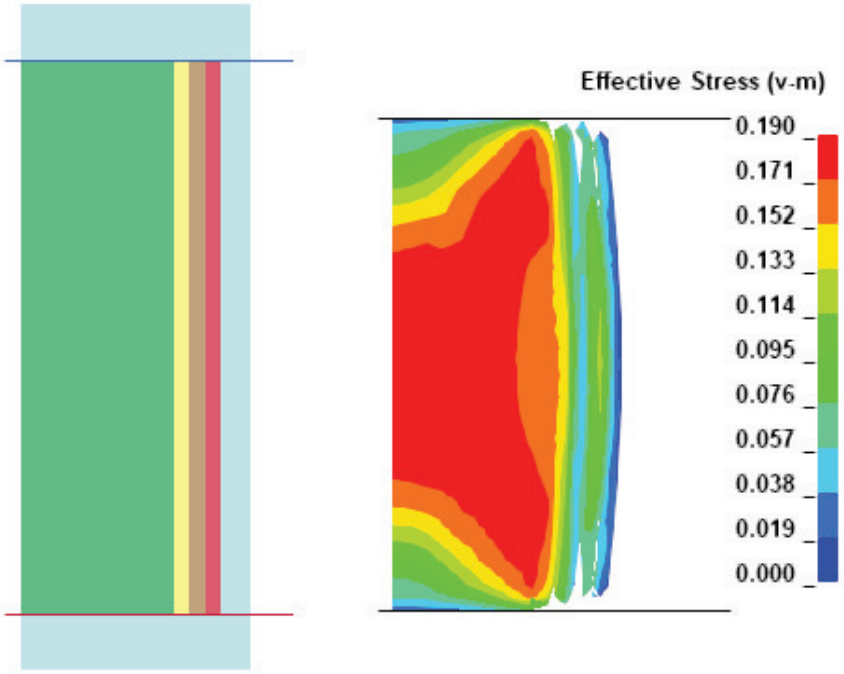

Figure D4. Multi-material FE model with the oxide scale.

Appendix E. Case of study: friction assessment.

Since friction is one the major disadvantages of the cylindrical compression test, it must be characterized carefully. To determine the friction as close to the actual forging process as possible, ring test was carried out as follows: the standard designation is 38MnVS6, the material's plastic flow was previously described in Chapter 3. The specimens were machined from an as-received raw bar, giving the following dimensions 80:40:27 mm (outer diameter, inner diameter, and height) to keep the geometry aspect ratio 6:3:2. The samples were heated by induction and held for 30 seconds, then were compressed in a hydraulic press with 10 MN in force capacity, shown in Figure E1. Table E1 shows the experimental parameters and its levels.

Table E1. Experimental conditions and levels.

Level	Temperature [°C]	Tool speed [mm/s]	Deformation %
High	1200	150	80
Medium	1100	80	60
Low	900	20	40

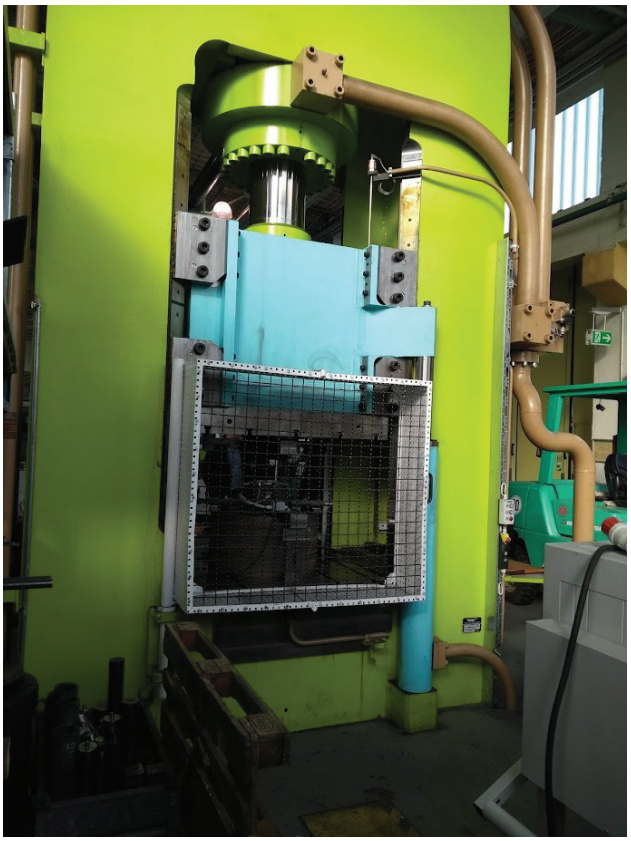

Figure E1. 10 MN Servo hydraulic press.

The friction is determined by reverse engineering, using a Finite Element Model, performed in QForm. The RCT has originally expressed the hypothesis that the inner diameter changes through the axial deformation depends only on friction. However, nowadays, by using FE and more advanced measurement equipment, it is possible to state more complex and realistic hypotheses; for instance, the load-stroke was measured during the experiment, and since these data are output from the FE simulation as well, we can compare the results.

Several friction values (*m*) were tried in numerical simulations to determine the best fit for the whole dataset. Some of these values are shown in Figure E2 for different friction factors as well as the heat conduction coefficients C (W/K*m^2), even though this former was not measured during the experiment. The numerical results exhibit a closeness among them, and the experimental results are scattered in small clusters. To obtain more insight on this behavior, additional experiments were carried out in a servo-hydraulic press with 20 KN at the same temperatures, i.e., 900, 1100 and 1200°C but with speeds of 40, 90, and 140 mm/s.

For these additional experiments, small size rings (labeled as "small") were used: OD9: ID4.5: H3 mm, to keep the same aspect ratio as the largest size rings. The tools used for both experiments were manufactured using the same material and processes as the actual hot forging operation. Both experiments with large and small size rings are plotted with the numerical results in Figure E2.

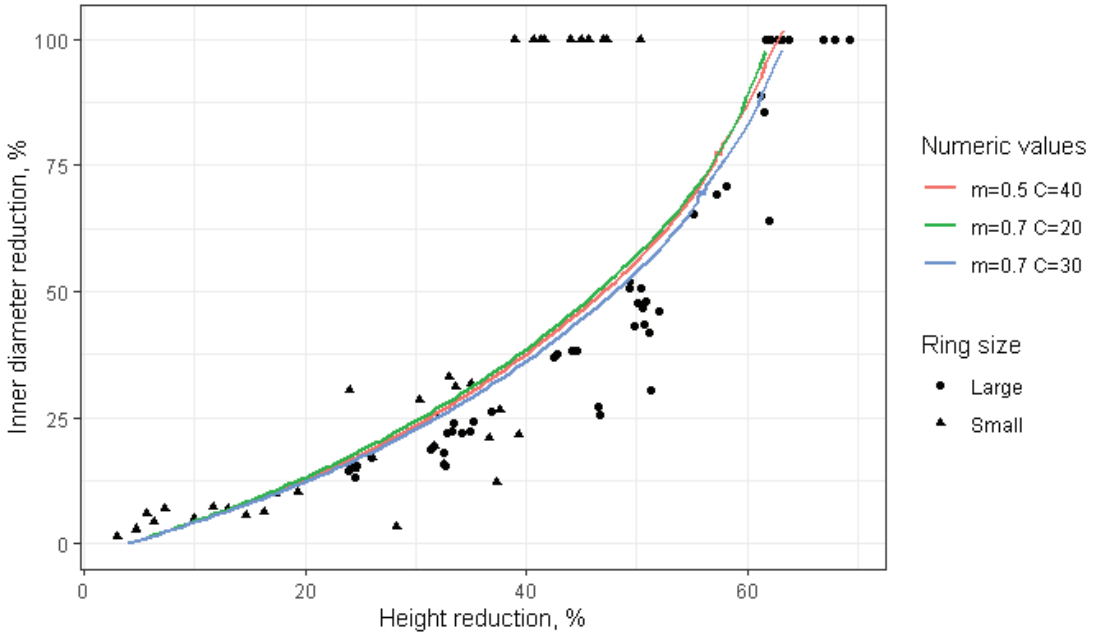

Figure E2. Numeric and experimental results (large and small sizes) for inner diameter reduction.

The friction factor was determined to be 0.7, and the coefficient of heat transfer was established as 30 $W/K*m^2$. This former parameter was not measured directly from the experiments, but it is a standard input parameter in FE simulation during the contact set-up. It is notorious the difference between some experimental and numeric results; however, the practical objective is to fit the best curve for most of the points. Another approach could be to establish a fit separately per conditions, e.g., fit a friction coefficient for each temperature and or velocity. This approach may be more accurate, but it is also more complicated and expensive from the computational viewpoint. In addition, it requires that computational codes are prepared to receive such kind of inputs.

Appendix F. Calculated Stress Comparison against the Experimental.

This appendix shows the plot for all experimental conditions as follows: for each model (H-S and J-C), the calculated stress is plotted against the experimental value (blue dots), in addition, a linear regression is shown (red line). Since the stress values are calculated at the same experimental strain, this means that the perfect output should be a perfect line, i.e., 100 % correlation.

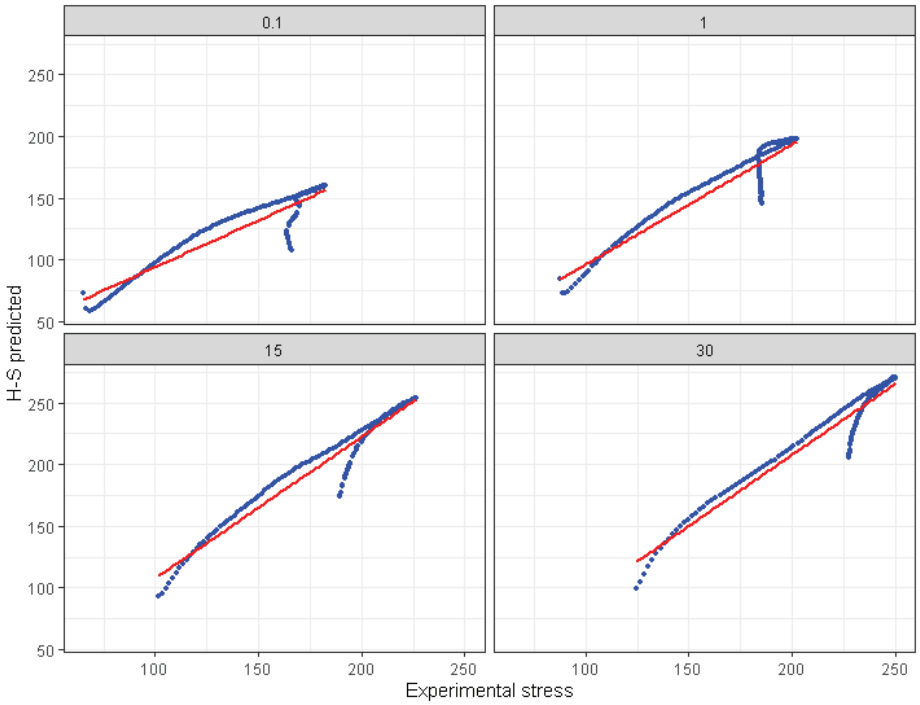

Figure F1: Stress values predicted by H-S model at 900°C.

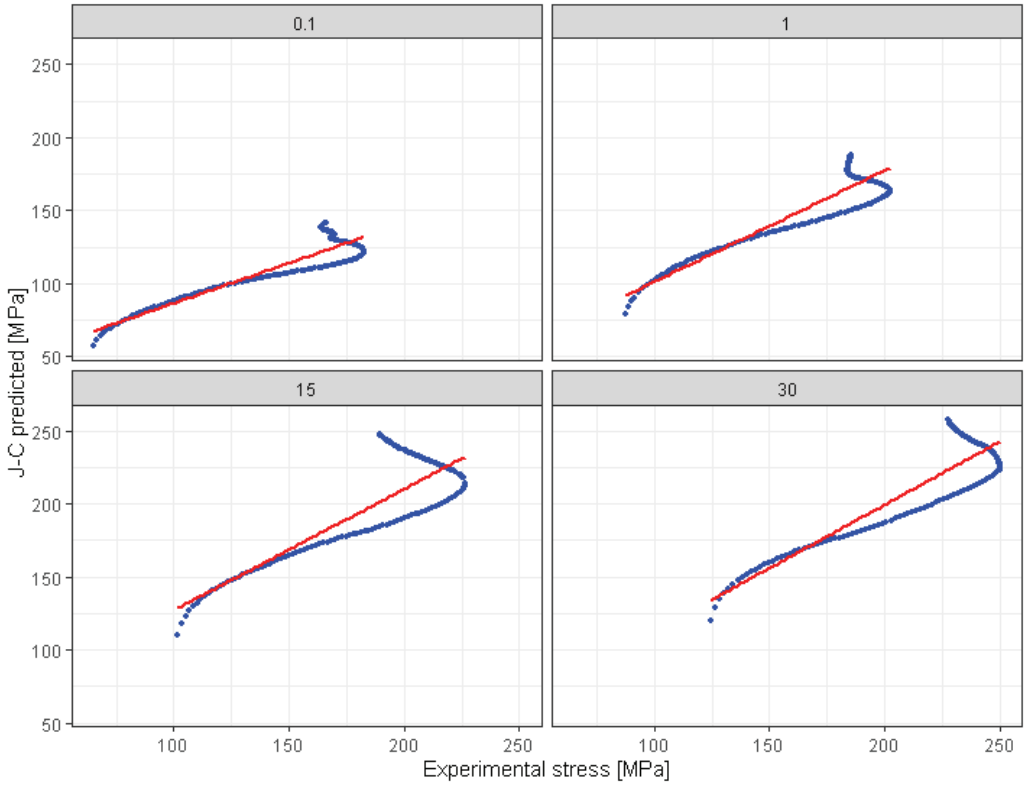

Figure F2: Stress values predicted by J-C model at 900°C.

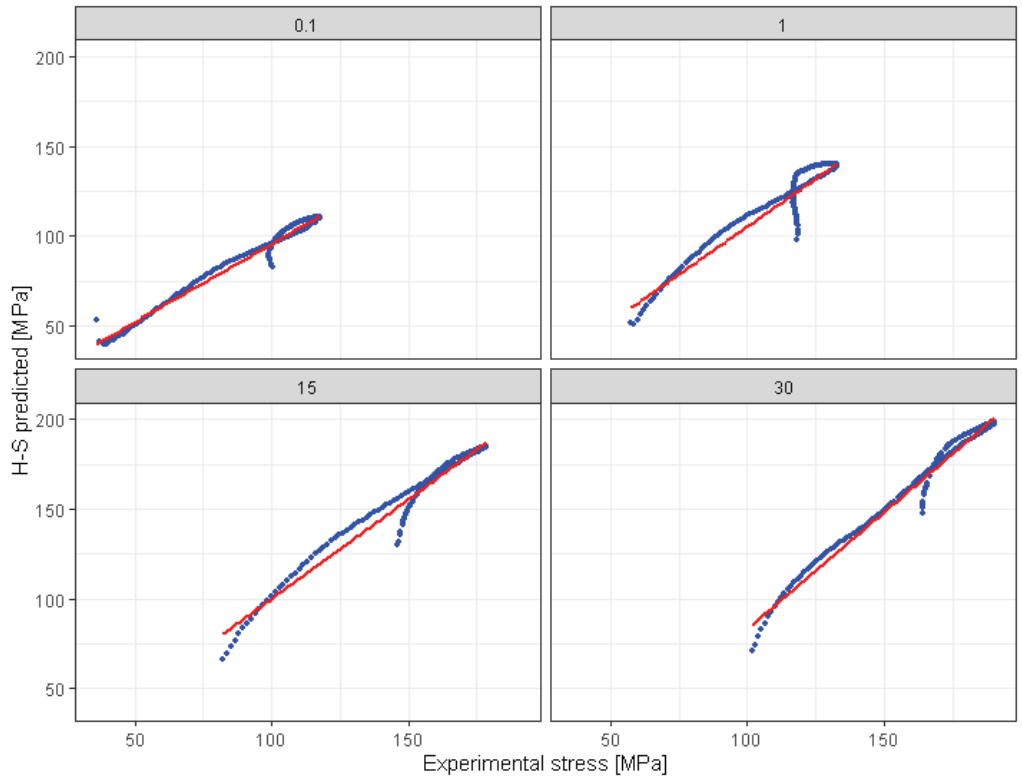

Figure F3: Stress values predicted by H-S model at 1000°C.

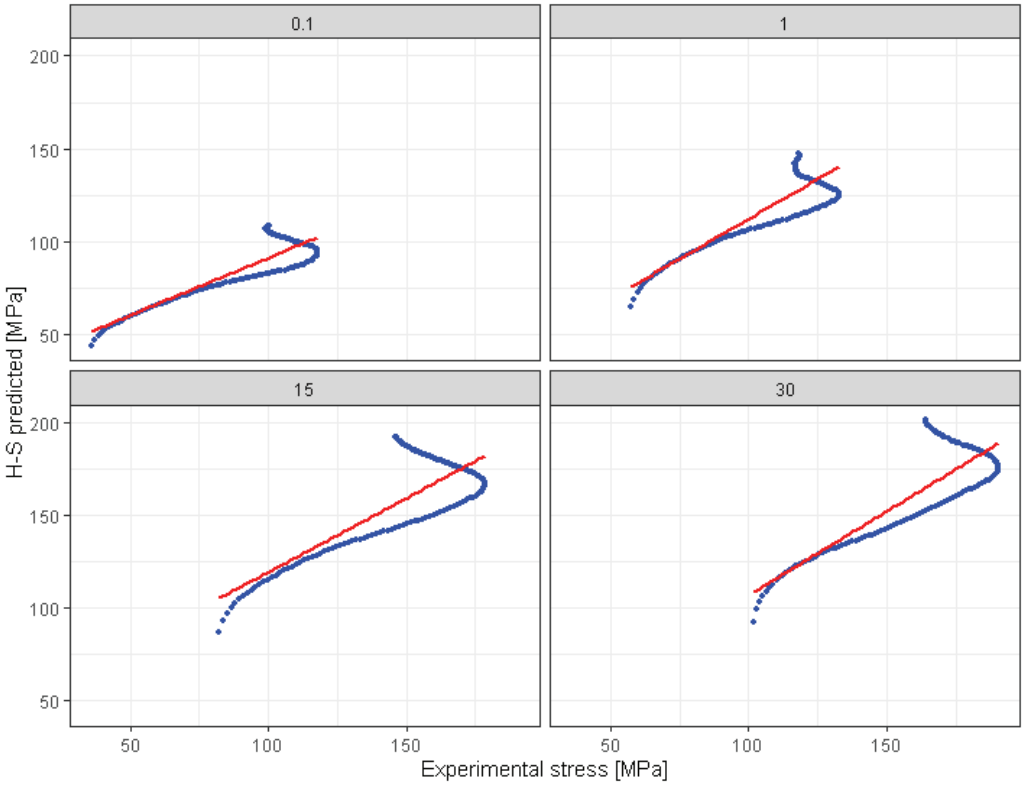

Figure F4: Stress values predicted by J-C model at 1000°C.

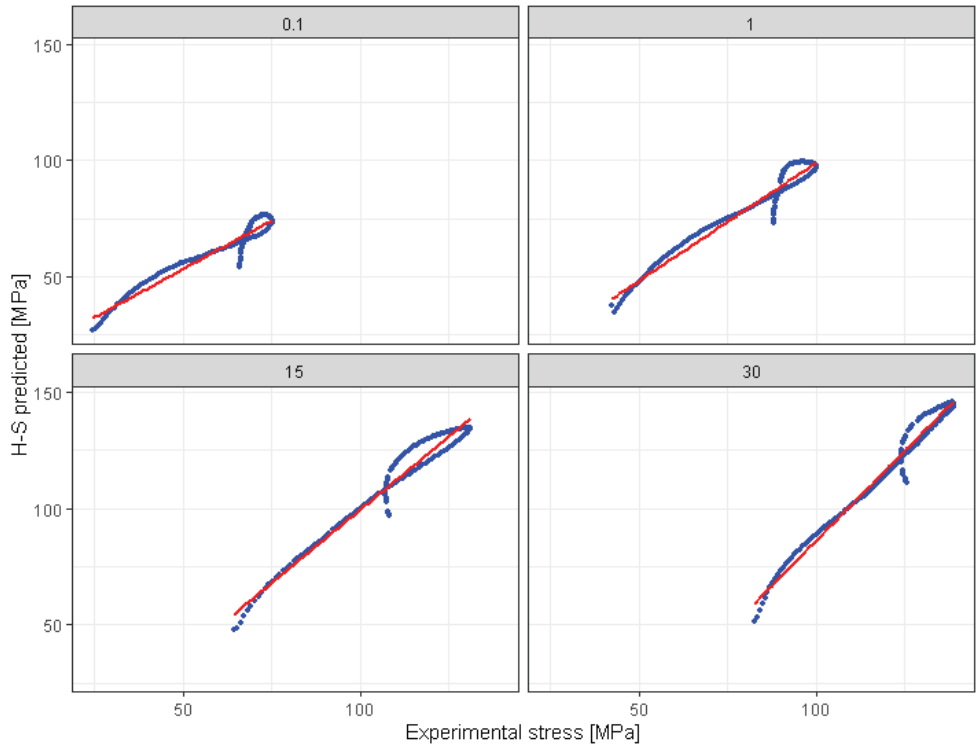

Figure F5: Stress values predicted by H-S model at 1100°C.

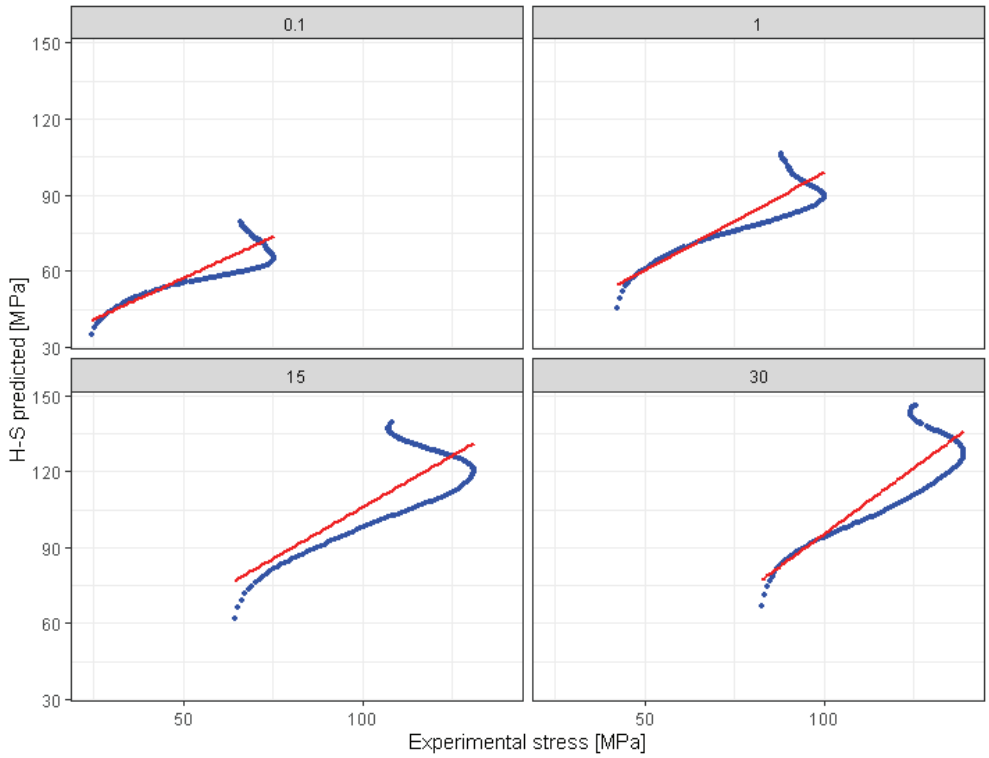

Figure F6: Stress values predicted by J-C model at 1100°C.

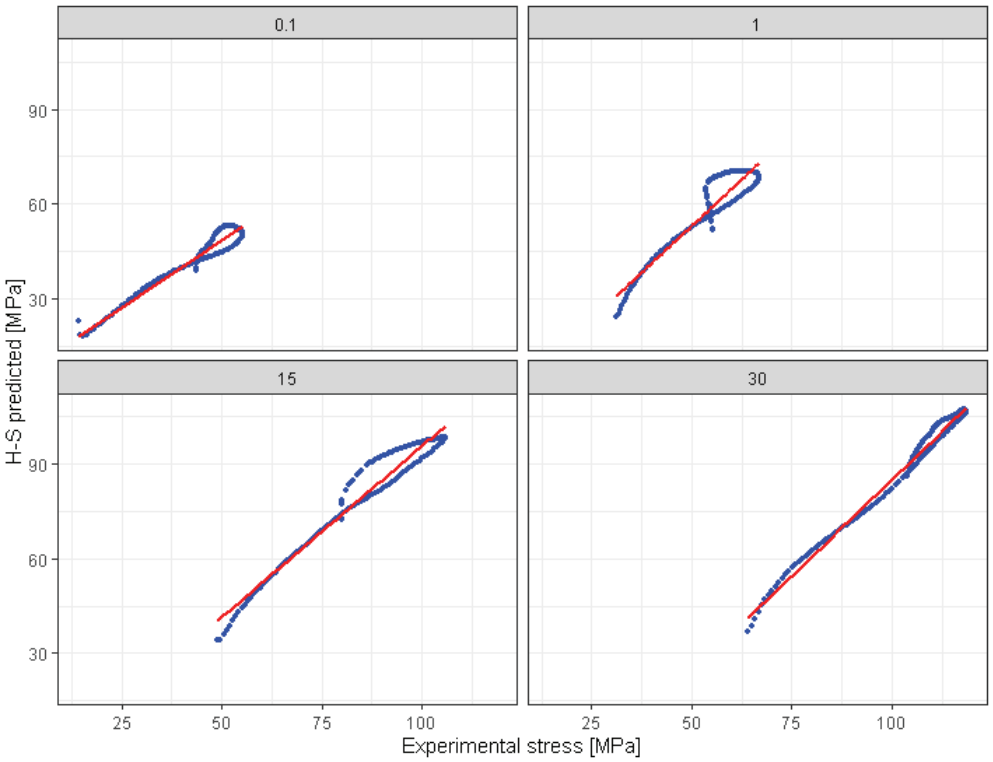

Figure F7: Stress values predicted by H-S model at 1200°C.

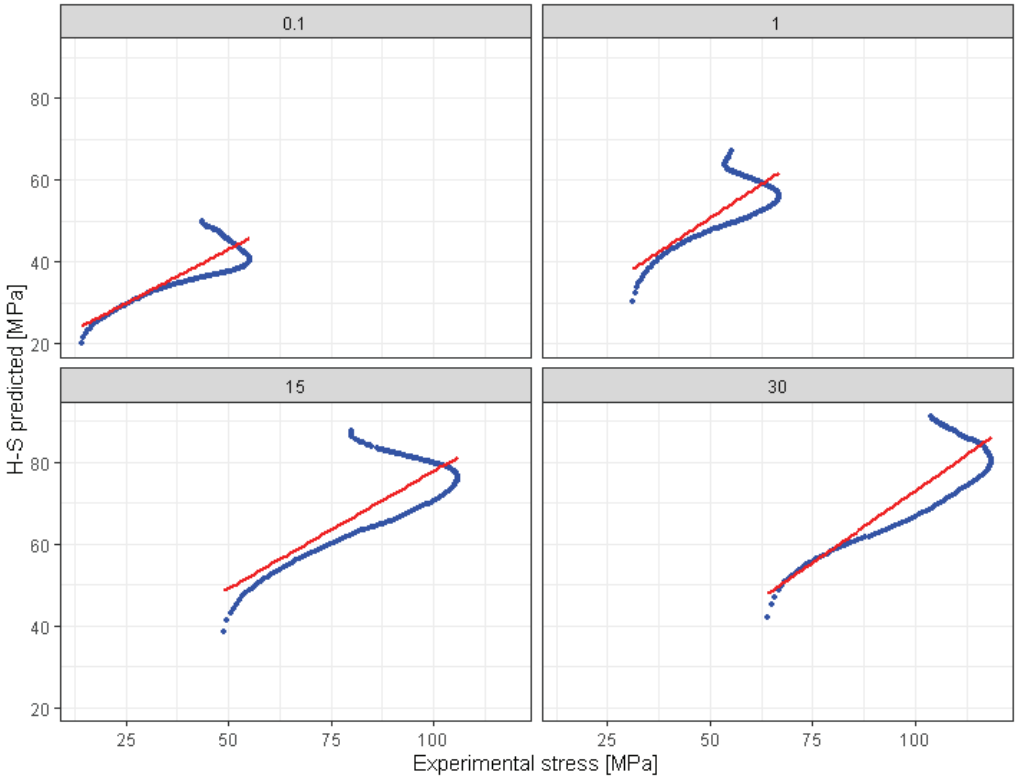

Figure F8: Stress values predicted by J-C model at 1200°C.